学位申請論文

Study on Effect of Elemental Substitution on Surface and Electronic States in Transition Metal Dichalcogenides

(遷移金属ダイカルコゲナイドの表面および電子状態への元素置換効果の研究)

by

Yuita Fujisawa

A dissertation submitted in partial satisfaction of the requirements for the degree of

Doctor of Science

in

Physics

in the

GRADUATE DIVISION

of the

TOKYO UNIVERSITY OF SCIENCE

March, 2018

Abstract

Effect of elemental substitution on surface and electronic states in transition metal dichalcogenides (TMDCs) were studied by means of scanning tunneling microscopy and spectroscopy (STM/STS). 1T-$IrTe_2$ and 1T-TaS_2 are TMDCs that show phase transitions involving the formation of the supermodulations (SMs) with different origins. The SMs are suppressed gradually by increasing the amount of substituted elements (Pt for Ir and Fe for Ta, respectively). Furthermore, superconductivity emerges when the phase transition is completely suppressed. Thus, these materials provide a unique playground to investigate relationship between the SM and superconductivity. Although many studies have been done, it is still unclear what is the role of the dopants and how the SM vanishes approaching to superconducting state. To clarify these issues, STM/STS observations of $Ir_{1-x}Pt_xTe_2$ and $Ta_{1-x}Fe_xS_2$ were performed.

$IrTe_2$ undergoes a structural phase transition involving formation of a uniaxial (stripe) SM at 280 K. STM observation in $Ir_{1-x}Pt_xTe_2$ captured how the SM evolves with increasing Pt concentration: The sample that shows the phase transition exhibits the same SM as that observed in $IrTe_2$, while superconducting $Ir_{1-x}Pt_xTe_2$ shows an unexpected domain structure instead of the SM. STM observation also identified the location where Pt is substituted. STS measurement on individual Pt site revealed the primary role of Pt is to induce structural distortion. The structural distortion seems to induce the domain structure observed in the superconducting sample. The relationship between the domain structure and emergence of superconductivity was discussed.

TaS_2 undergoes a phase transition to commensurate charge density wave (CCDW) state at 200 K. In the CCDW state, a regular triangular lattice of clusters composed of 13 Ta atoms, so called David-star clusters appears. Simultaneously, it transforms into a Mott insulating state owing to strong correlation between each electron located as the center of the David-stars. STM observation in $Ta_{1-x}Fe_xS_2$ revealed the different configurations of the David-stars depending on the Fe concentration. Especially, in the sample in which the CCDW transition is suppressed, the CCDW is divided into domains. STS measurements revealed that the domains show a Mott nature, while the domain walls does not. Region corresponding to the walls increases approaching to the concentration in which superconductivity appears. Thus, this indicates that the domain wall is essential for the emergence of superconductivity. The relationship between the domain walls and superconductivity was discussed.

List of acronyms

STM/STS	scanning tunneling microscopy/scanning tunneling spectroscopy
ARPES	angle resolved photoemission spectroscopy
DOS	density of state
LDOS	local density of state
CDW	charge density wave
SM	supermodulation
E_F	Fermi energy
T_c	superconducting transition temperature

Contents

List of Figures

Chapter 1

Introduction

Transition metal dichalcogenides (TMDCs) are quasi two dimensional materials and have been attracted much attentions for half a century, because of rich variety of physical phenomena. One example is the formation of the supermodulation (SM) with a larger period than the original lattice. Another example is superconductivity. Recently, several kinds of TMDCs are found to show superconductivity by elemental substitution, though only a few TMDCs show superconductivity without elemental substitution. The superconductivity appears when SM is suppressed by elemental substitution. Thus, we got chances to investigate the relationship between the SM and superconductivity. There are some questions to be solved about the elemental substitution in TMDC : How the SM is destroyed and what is the role of substituted element, and which is essential for the emergence of superconductivity.

In this chapter, I will briefly overview the crystal structure and electronic states of TMDCs, two qualitative pictures to understand the formation of SM in TMDCs, and superconductivity induced by elemental substitution in TMDCs for introduction. After that, I will present the objects in this thesis.

1.1 Transition metal dichalcogenide

A transition metal dichalcogenide (TMDC) is composed of a transition metal and chalcogen atoms with a morr ratio of 1:2. Several combinations of transition metals and chalcogen atoms are possible as shown in Fig. 1.1. TMDCs show several layered crystal structures. Typical structures are shown in Fig. 1.2(a) and (d). Here, each red (blue) ball represents a transition metal (chalcogen) atom. The crystal structure shown in Fig. 1.2(a) is called as $1T$ polytype. In this polytype, a layer is composed of the edge sharing octahedra as shown in Fig. 1.2(c). Figure 1.2 (b) shows the top view. Each transition metal layer and chalcogen layer forms a regular triangular lattice. Another shown in Fig. 1.2(d) is called as $2H$ polytype. In this polytype, a layer is composed of the edge sharing prisms as shown in Fig. 1.2(f). Figure 1.2(e) shows the top view. Each transition metal layer and chalcogen layer also forms a regular triangular lattice. There are the other types of polytype which is formed different stacking of the layer, such as $4H_{\mathrm{b}}$ polytype that has alternate stacking of T and H layer.

The electronic states of the T type TMDCs can be elucidated from the crystal field effect in general. Figure 1.3 shows the energy level of d electrons. While five d orbitals are degenerated in free space, the five orbitals split into two

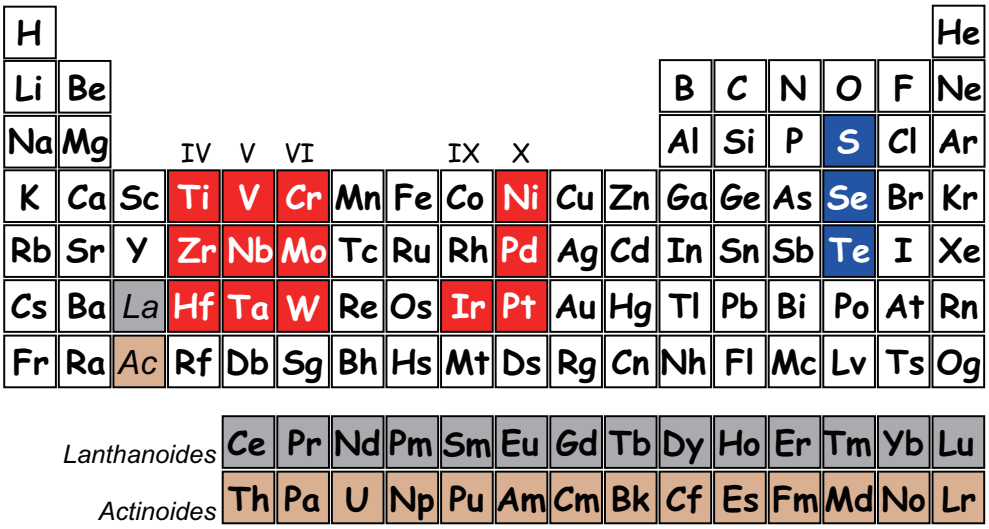

Figure 1.1: The periodic table. Each transition metal with red color forms the crystal structure as shown in Fig. 1.2 with chalcogen. The elements with blue color indicate the chalcogen.

orbital groups, t_{2g} and e_g orbitals in the octahedral coordination. The energy of e_g orbitals is higher than that of the t_{2g} orbitals, because e_g orbitals are directed to the chalcogen atoms, and repel the p orbitals of chalcogen. Transition metals in TMDCs often have one to six electrons in d orbitals. This indicates that t_{2g} orbitals are partially filled, leading to metallic behavior in general. In the case of $1T$-$IrTe_2$ and $1T$-TaS_2, which are studied in this thesis, assuming the valence number of Ir and Ta is 4+, the number of electrons in the t_{2g} orbital in Ir and Ta is five and one, respectively. This implies that both materials show metallic behavior. In fact, these materials are metallic at high temperature. With decreasing temperature, both materials undergo a phase transition involving the formation of a supermodulation (SM).

1.2 Supermodulation in TMDCs

One of the remarkable features in TMDCs is the spontaneous formation of supermodulations (SMs) in which the lattice and the density of electrons show a larger periodicity than the original lattice constant. In the formation of the SM, the interaction between electrons and the lattice, *i.e.* electron phonon coupling (EPC) is important. Basically, the formation of the SMs can be classified in two classes; weak coupling and strong coupling. In the weak coupling limit, the formation of SM is described by the theory by Peierls. The resulting SM is called “charge density wave” (CDW). On the other hand, in the strong coupling limit, SM can be recognized as qualitative picture like ”dimerization”. In this section, I will describe about these formation of SMs.

1.2.1 Weak couplig; Peierls transition

One of the most famous origins for SM formation is the Peierls transition predicted by R. Peierls in 1930s. This prediction is based on low dimensionality of the Fermi surface of a material. As a simplest model, we will think of

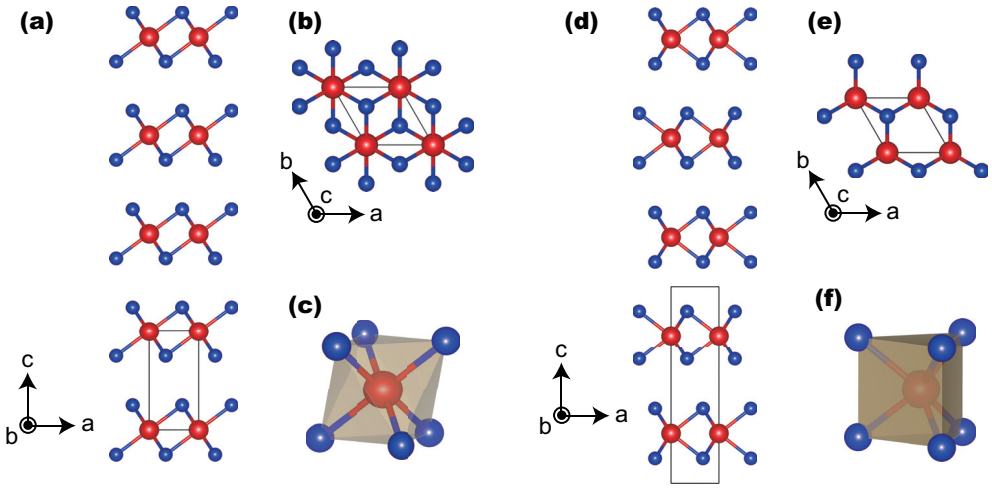

Figure 1.2: Typical crystal structure of TMDCs. (a), (d) Crystal structures of 1T and 2H polytypes. (b), (e) Top view of the crystal structures of 1T and 2H polytypes. (c), (f) A transition metal and surrounding six chalcogen atoms of 1T and 2H polytyps.

a system composed of one dimensional (1D) chain with one electron per an atomic site (such as $2s^1$ electron in ^{3}Li chain or $3s^1$ electron in ^{11}Na chain), as shown in Fig.1.4(a). The band dispersion in the system is shown as gray line in Fig.1.4(c). Because one electron exists in an orbital, the Fermi energy (E_F) is located in the band, indicating that the system is metallic. Fermi surface in this system is shown in Fig. 1.5(a). When two part of the Fermi surfaces (two Fermi sheets at $k = \pm k_F$, in the present case) is well nested, charge susceptibility at $2k_F$, $\chi(2k_F)$, is enhanced, as shown in Fig. 1.4(d).

Because,

$$\rho(Q) = -V_Q \chi(Q), \tag{1.1}$$

where $\rho(Q)$ is density of electrons with a wave vector of Q, and V_Q is periodic potential with a Q, the enhancement of

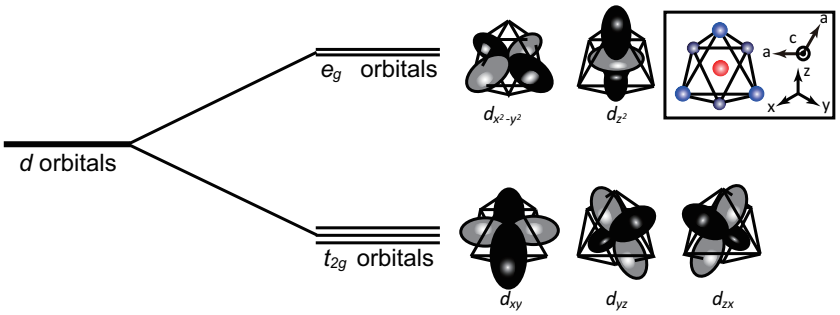

Figure 1.3: Schematic drawing of d orbitals in octahedral coordination of chalcogen atoms. Five orbitals are split into three orbitals with lower energy and two with higher energy. The three (two) orbitals are called as the t_{2g} and the e_g orbitals.

$\chi(2k_F)$ leads to a finite electronic modulation with $k = 2k_F$.

When the electronic density modulation with $k = 2k_F$ is formed, an energy gap opens at E_F, as shown in Fig.1.4(c). If the energy gain due to the formation of the energy gap overcompensates the Coulomb energy between electrons and elastic energy in the lattice, the electronic density modulation becomes stable. This SM owing to the Fermi surface nesting is called as charge density wave (CDW) in general. I use this word "CDW" as the SM formed by Peierls mechanism in this thesis.

When the system is two dimensional with one electron per an atom, CDW doesn't seem to be stable, because of bad nesting condition (Fig. 1.5(b)) and resulting no remarkable peak in $\chi(Q)$ (Fig. 1.4(d)) in general. However, if the shape of the Fermi surface is so special that the large area on the Fermi surface nests, CDW becomes stable even in two dimensional materials. Such an example is a typical TMDC, $1T$-TaS_2. Figure 1.5(c) shows the Fermi surface of $1T$-TaS_2 in the normal state. There are three nesting vectors as shown in black arrows. Indeed, $1T$-TaS_2 undergoes a CDW transition from the normal state to an incommensurate CDW state with the nesting vector.

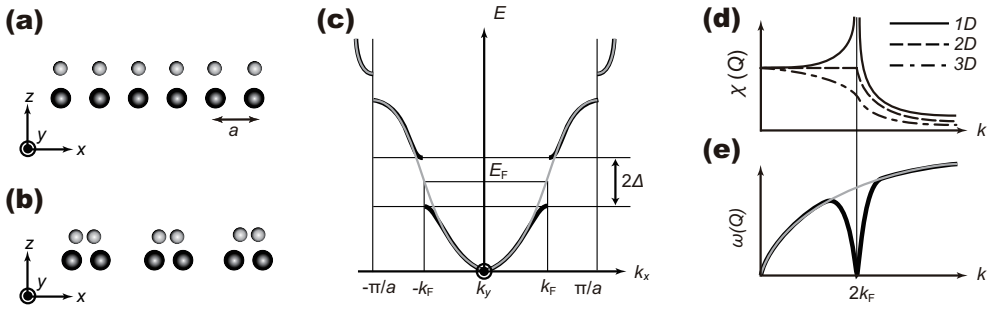

Figure 1.4: Schematic illustrations associated with the Peierls transition. (a) Schematic of 1D atomic chain with one electron per atomic site. Each black and gray ball represent an atom and an electron. (b) A resultant CDW of 1D atomic chain predicted by Peierls. (c) Band dispersion of the system. Gray line indicates a band dispersion in the normal state as shown in (a). Thick black line indicates a band dispersion in the CDW state as shown in (b). (d) Charge susceptibility dependent on wave vector and the dimensionality. (e) Phonon dispersions. Gray and thick black lines indicate the dispersions well above the transition temperature and at the transition temperature, respectively.

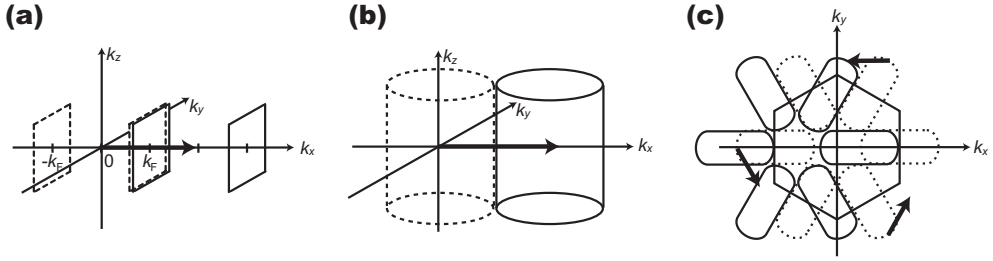

Figure 1.5: Schematic illustrations of Fermi surfaces. (a) Parallel Fermi surface of 1D atomic chain, as shown in Fig.1.4(a). (b) Cylindrical Fermi surface. In this case, Nesting is not so good. (c) Schematic of Fermi surface of a normal state in $1T$-TaS_2. Thick black arrows in each figure indicate the nesting vectors. Hexagon in this figure indicates first Brillouin zone of this material.

The Peierls transition can be treated quantitatively by the mean field theory. The Hamiltonian (so-called Fröhlich Hamiltonian) leads to several important aspects of the Peierls transition.

One is the condition for the SM formation;

$$\frac{4{g_Q}^2}{\hbar\omega_Q} > \frac{1}{\chi_(Q)} \tag{1.2}$$

, where ω_Q is phonon dispersion as a function of Q and g_Q is an electron phonon coupling constant. (In the following, I assumed g does not depend on Q). This apparently indicates that large $\chi(Q)$ at the CDW wave vector (Q_{CDW}) is needed for the CDW formation. Because $\chi(Q)$ is directly related to the nesting condition, the requirement of inequation (1.2) is consistent with the nesting picture introduced above.

One can also obtain the change in phonon dispersion from the Fröhlich Hamiltonian due to the EPC. As shown in Fig. 1.4(e), Ω_Q at $Q = Q_{\mathrm{CDW}}$ reduces when temperature approaches to the CDW transition temperature (T_{CDW}). This softening of phonon is called as Kohn anomaly and can be considered as a precursor of the CDW formation.

In addition to the lattice displacement u_Q due to the CDW formation, and electronic modulation $\rho(Q)$ at Q_{CDW}, the energy gap due to CDW formation (CDW gap, Δ) is also an order parameter in the CDW state. The energy gap Δ is related to T_{CDW} in the mean field theory as

$$\frac{2\Delta}{k_{\mathrm{B}}T_{\mathrm{CDW}}} = 3.5 \tag{1.3}$$

The value 3.5 is same as that in the BCS theory in superconductivity.

1.2.2 Strong coupling; Q dependent electron phonon coupling

Another origin for the SM formation is the strong EPC depending on Q, which is more appropriate for explaining the origin of the SM formation in TMDCs. Although weak EPC is required for the CDW formation in the framework of the Peierls transition, strong EPC leads another picture of the SM formation as follow.

Several theoretical studies which discuss the effect of the strong EPC claimed that ω_Q becomes soft in wide Q range and $\chi(Q)$ shows broad peak in Q space [1, 2]. Furthermore, order parameters of the CDW, including Δ, u_Q, and $\rho(Q)$ become large when the EPC is enhanced [3]. The increase in Δ indicates that electrons near the E_{F} are gapped in wide k space as shown in Fig. 1.6. In the extreme limit of the strong EPC, Δ opens in the entire Brillouin zone, as shown in Fig. 1.6(c). The resultant $E - k$ relations look like those of a bonding and an anti-bonding state in terms of chemistry [5, 6]. Thus, in line with this idea, “dimerization” can be understand as one of the examples in the strong EPC coupling. If “dimerization” realized with a wave vector Q, this called ”partial dimerization”.

Because of the difference in the mechanism for the SM formation, the expected period of SM is different in the weak and strong EPC limit. In the weak coupling limit, the origin of CDW formation is attributed from the Fermi surface nesting. Thus, the CDW wave vector Q_{CDW} is determined by k_{F}. This indicates that the periodicity of the CDW tends to be incommensurate because k_{F} is determined by the number of electrons available. In the strong coupling limit, on the other hand, a local chemical bonding picture seems to be more appropriate as shown in Fig. 1.6(c). Because the atoms tend to form pairs with shortened bond, like “dimer”, the CDW tends to be commensurate with respect to the original lattice.

The importance of strong EPC in TMDCs has been studied extensively recently. One of such systems is 2H-

$NbSe_2$, which shows a SM below 30 K. Although, the SM in $2H$-$NbSe_2$ had been thought that it was caused by Peierls mechanism, inelastic X-ray scattering measurements in $2H$-$NbSe_2$ revealed the temperature dependence of $\omega(Q)$ which has depression in wide Q range. This is in good agreement with the theoretical calculation by the model with Q dependent strong EPC[7]. Furthermore, STM observation above T_{CDW} revealed the existence of the SM in a vicinity of Se vacancies with short coherence length [8]. This is indicative of short coherence length expected from the strong EPC. Thus, the strong EPC is thought to be important in the formation of the SM in $2H$-$NbSe_2$.

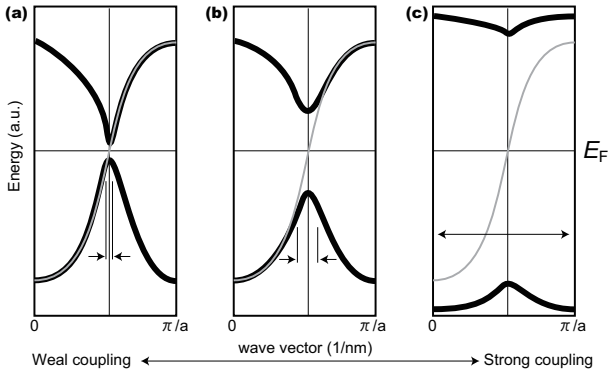

Figure 1.6: Evolution of band dispersions of a CDW state with different EPC constant [4]. Arrows in each figure represents the width of the gapped wave vector.

As a summary of this section, the differences of these SMs are summarized in Table 1.1.

Table 1.1: Comparison between weak and strong coupling induced CDWs [3]

	weak coupling	strong coupling
CDW amplitude	small	large
CDW gap	small	large
Electronic energy gain	obtained from near k_F	obtained from entire Brillouin zone
coherence length	long	short
CDW periodicity	incommensurate	commensurate
Qualitative picture	Fermi surface nesting	local chemical bonding

1.3 Superconductivity in TMDCs

A few TMDCs show superconductivity. Typical one is $2H$-$NbSe_2$ with T_c of 7 K [9]. Because the material also shows a SM below 30 K, many researches have been done to investigate how they coexist, especially in reciprocal space [10]. Recently, the emergence of superconductivity was reported when an element is substituted or intercalated to TMDCs. Examples of such superconductors are Pt substituted $IrTe_2$, Fe substituted TaS_2, and Cu intercalated $TiSe_2$ [11–13]. Without elemental substitution, these materials undergo phase transitions involving the formation of SMs with different wave vectors. The transition temperature decreases as increasing the amount of the elemental substitution. At the

concentration where the formation of the SM is completely suppressed, superconductivity appears at approximately 3 to 5 K in these materials. Further substitution suppresses the T_c. The behavior of T_c against concentration of substituted element is summarized in Fig. 1.7(a) to (c). Each figure is called "electronic phase diagram". They show "superconducting dome", which is also seen in high T_c cuprates and iron based materials. Owing to the discoveries of superconductivity in the TMDCs, intensive study on the relation between the SMs and superconductivity by elemental substitution became possible in addition to the study of the prototypical TMDCs such as 2*H*-$NbSe_2$.

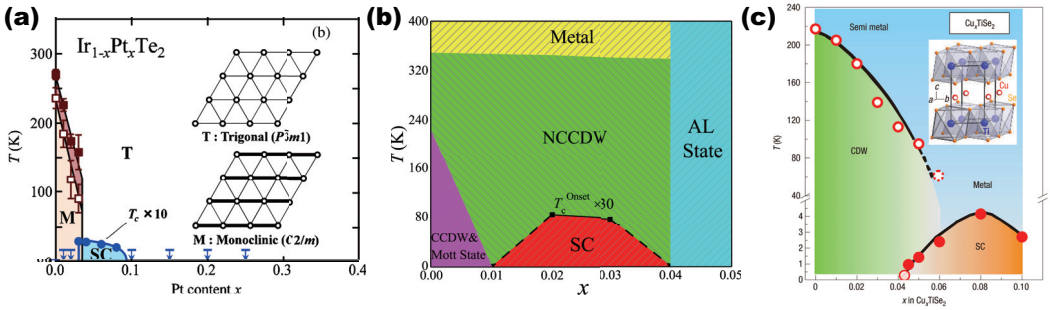

Figure 1.7: Phase diagrams of the TMDC superconductors. (a) to (c) show that of Pt doped $IrTe_2$, Fe doped TaS_2, and Cu intercalated $TiSe_2$, respectively [11–13].

1.4 Objects and organization of this thesis

There are some reports on experimental and theoretical studies of these superconductors. However, there are some questions to be resolved. One is how the SM is destroyed as increasing substituted elements. In order to observe the change of the SM with the substitution in real space, scanning probe microscopy is the appropriate experimental tool.

Another is the role of the dopant, which is essential for the emergence of superconductivity. In general, substituted elements provide both of extra carrier and structural strain owing to the difference in the valence number and ionic radius, respectively. There exist many experimental techniques to probe these effect individually. However, scanning tunneling microscopy and spectroscopy can probe both effects directly. Thus, in order to address these issues, I performed STM/STS measurements in the superconducting TMDCs, Pt substituted $IrTe_2$ ($Ir_{1-x}Pt_xTe_2$) and Fe substituted TaS_2 ($Ta_{1-x}Fe_xS_2$) with several x concentration. The organization of this thesis is as follows.

In chapter 2, I will introduce details of STM/STS experiments.

In chapter 3, I will discuss the results in $Ir_{1-x}Pt_xTe_2$. $IrTe_2$ showed a SM, which is believed to be owing to the partial dimarization as described in the previous section. STM observation of the SM with different x suggested that the scenario of the partial dimerization is appropriate for the origin of the SM. A sample which shows superconductivity below the measurement temperature shows an unexpected domain structure. This structure seems to be related to the emergence of superconductivity. I also succeeded in identifying individual dopants in STM images. I will also present the STS results and discuss the role of the domain structure caused by Pt substitution and its relationship to the emergence of superconductivity.

In chapter 4, I will discuss the results in $Ta_{1-x}Fe_xS_2$. TaS_2 undergoes successive CDW transitions. Its ground state is a Mott insulating state coexisting with a commensurate CDW state. In this chapter, the melting process from the Mott state to metallic (superconducting) state through Fe substitution is discussed. While pristine TaS_2 showed regular array of cluster composed of 13 Ta atoms (so called David-star cluster) in the STM image, in the sample that shows neither the Mott nor superconducting transition down to 2 K, regular array of the David-stars are divided into domains by domain walls. The electronic structures of the David-stars in the domain and on the wall were quite different each other: electronic states in the domains show Mott like feature, while the walls do not. The STS measurements in the sample that shows superconductivity below measuring temperature revealed the inhomogeneous electronic structure. The inhomogeneity was revealed to be due to the two types of tunneling spectra observed at the domains and the walls in the domain structure. Because the tunneling spectra observed at the walls become dominant as increasing Fe concentration, the region which shows the spectra is responsible for the emergence of superconductivity. I will discuss the role of the walls and its relationship to the emergence of superconductivity.

In chapter 5, I will summarize this thesis.

Chapter 2

Scanning tunneling microscopy and spectroscopy

Scanning tunneling microscope was invented by Binning and Rohrer in 1982, for which they won the 1986 Novel Prize in Physics [15]. The instrument enables us to investigate surface geometry of samples with atomic resolution. The surface observation with scanning tunneling microscope is called as scanning tunneling microscopy (STM). [1] This capability of STM is based on the fact that the tunneling current between a tip and a sample depends exponentially on the separation between them, which is typically a few Å. Moreover, because the tunneling current is proportional to the integrated local density of state (LDOS) from the Fermi energy to the set point energy, one can obtain the LDOS with atomic resolution by means of scanning tunneling spectroscopy (STS). In this section, I describe an introduction of tunneling current, fundamental components of the instrument, data acquisition and processing of STM/STS measurements, and experimental setup in our laboratory.

2.1 Tunneling current

Fundamentally, STM consists of a tunneling junction between a sharp conducting tip and a flat conducting sample surface with separation of a few Å, as shown in Fig.2.1(a). Assuming that the tunneling barrier is square, we can obtain tunneling probability $|M|^2$ through the barrier using WKB approximation as

$$|M|^2 \propto \exp\left(-2\frac{\sqrt{2m\phi}}{\hbar}d\right) \tag{2.1}$$

where m is the mass of an electron, d is the separation between the tip and the sample surface, and ϕ is the height of barrier, which is actually average of the work functions of the tip and the sample.

When a bias voltage is applied to the junction, tunneling current flows between the tip and the surface through tunneling barrier. The actual barrier is vacuum or some gasses. When the sample is biased by a voltage V with respect

[1] In this thesis, both scanning tunneling microscope and scanning tunneling microscopy are abbreviated as STM customarily.

to the tip, the Fermi level of the sample is lowered with respect to that of the tip by eV as shown in Fig. 2.1(b), where e is the charge of an electron. In this case, the tunneling current from the tip to the sample is written with $|M|^2$ and the density of states of the sample (tip) N_{sample} (N_{tip}) as

$$I_{\text{tip}\to\text{sample}} = 2e \cdot \frac{2\pi}{\hbar}|M|^2 \cdot \int_{-\infty}^{\infty}[N_{\text{tip}}(E+eV)f(E+eV)] \cdot [N_{\text{sample}}(E)(1-f(E))]dE \tag{2.2}$$

where $f(E)$ is the Fermi distribution function.The factor of 2 is for spin. Note that the origin of the energy is fixed at the Fermi energy of the sample.

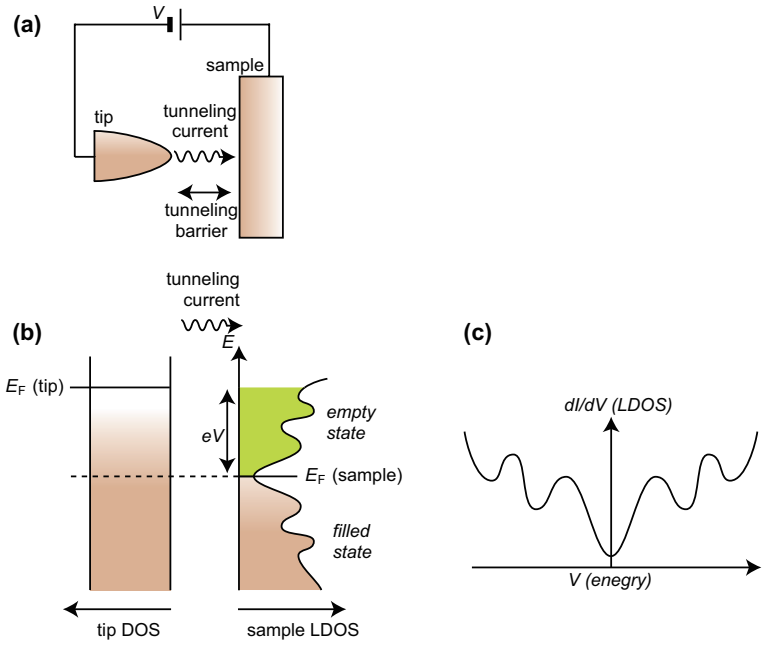

Figure 2.1: Schematics of the tunneling current (a) Schematic of a STM tip and a sample. A bias voltage V is applied to the sample, and the tunneling current flows from the tip to the sample through tunneling barrier. (b) Density of state of the tip and the sample. Because the bias is applied to the sample, Fermi energy of the sample becomes lower with respect to that of the tip. (c) Relationship between the applied bias voltage and dI/dV, which corresponds to that of energy and the LDOS, respectively.

There also exists tunneling current from the sample to the tip,

$$I_{\text{sample}\to\text{tip}} = 2e \cdot \frac{2\pi}{\hbar}|M|^2 \cdot \int_{-\infty}^{\infty}[N_{\text{tip}}(E+eV)(1-f(E+eV))] \cdot [N_{\text{sample}}(E)f(E)]dE \tag{2.3}$$

Thus the net tunneling current from the tip to the sample is

$$I = I_{\text{tip}\to\text{sample}} - I_{\text{sample}\to\text{tip}} = \frac{4\pi e}{\hbar}|M|^2 \cdot \int_{-\infty}^{\infty}[N_{\text{tip}}(E+eV)N_{\text{sample}}(E)] \cdot [f(E+eV)-f(E)]dE \tag{2.4}$$

Since $f(E+eV)-f(E)$ becomes zero except $0<E<eV$ at $T=0$, equation (2.4) can be reduced to

$$I=\frac{4\pi e}{\hbar}|M|^2N_{\mathrm{tip}}\int_0^{eV}N_{\mathrm{sample}}(E)dE \tag{2.5}$$

Here, N_{tip} is considered as a constant because the tip is usually made of a normal metal. At liquid Helium temperature (4.2 K), equation (2.5) is valid approximately. Finally, using the equation (2.1), the tunneling current becomes

$$I\propto\exp\left(-\frac{d}{\lambda}\right)\cdot\int_0^{eV}N_{\mathrm{sample}}(E)dE \tag{2.6}$$

Here, $\lambda=\frac{\sqrt{8m\phi}}{\hbar}$. Since the tunneling probability depends on d exponentially, the tunneling current is very sensitive to d. This high sensitivity leads STM to atomic resolution.

2.2 Measuring system

Figure 2.2 shows a schematic illustration of a measuring system of STM. Tunneling current that flows between a tip and a sample surface is amplified and is compared with "set current", which is set through PC. The difference is feedbacked by a feedback controller and high voltage is applied to a piezo for vertical motion to correct the tunneling current to the "set current". High voltage is also applied to scanner x and y to scan in x and y directions of the sample surface. The tunneling current I, the bias voltage V, and the tip position (x,y,z) are recorded by a computer through a data acquisition module.

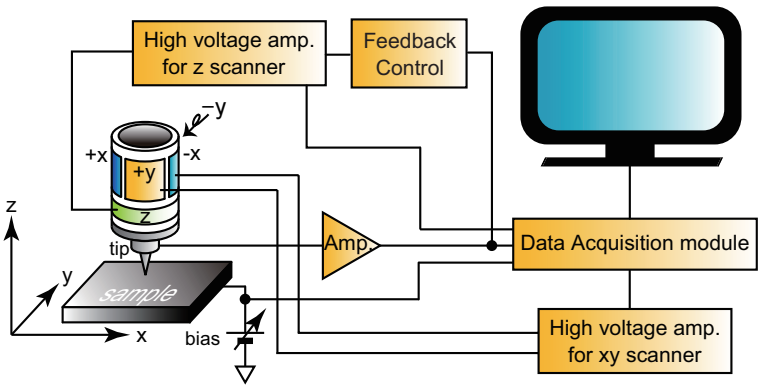

Figure 2.2: Schematics of overall apparatus of STM

2.3 Data acquisition and proccessing of STM/STS measurements

2.3.1 STM imaging

In general, there are two ways to obtain a topogaph image (STM image). One is *constant current mode* and the other is *constant height mode*. In the constant current mode, the feedback control adjusts separation z between an STM tip and a sample surface in order to set the tunneling current to a fixed value. In this mode, the sample surface geometry can be obtained by recording the voltage applied to a piezo for z motion as a function of (x, y). In the constant height mode, the voltage applied to a piezo for z motion is fixed at a value so that the height of the tip is constant. In this mode, the surface geometry can be obtained by recording the variation of the tunneling current I as a function of (x, y). All STM images in this thesis are obtained by the constant current mode, because it reduces the chance of the crush between the tip and the sample surface.

2.3.2 STS measurements

In STS measurements, I is measured as a function of V, after the feedback control is opened and the STM tip is held at a constant separation of z_0. The separation z_0 is determined so as to satisfy $I_0 = f(r, z_0) \int_0^{eV_0} N(r, E)dE$, where $f(r, z) = \frac{4\pi e}{\hbar}|M|^2 N_{\mathrm{tip}}$, $N(r, E)$ is the LDOS on a sample as a function of the position and the energy. Here, I_0 and V_0 are "set current" and "set bias", which can be set arbitrarily. Then, I is represented by

$$I(r, z_0, V) = f(r, z_0) \int_0^{eV} N(r, E)dE \tag{2.7}$$

Because $I(r, z_0, V)$ includes $N(r, E)$, one can obtain many maps involving the information of the electronic states of the sample from $I(r, z_0, V)$.

dI/dV conductance map

dI/dV can be obtained from (2.7) as

$$dI/dV(r, z_0, V) \equiv g(r, z_0, V) = f(r, z_0)eN(r, eV) \tag{2.8}$$

Thus, dI/dV is proportional to the LDOS. Experimentally, it is obtained by numerical differentiation of the $I - V$ characteristics. The numerical differentiation of the $I-V$ characteristics was done by using a laboratory-made program, "STS analyzer". By measuring the $I - V$ characteristic (shown in Equation 2.7) at each r, one can obtain a LDOS (dI/dV) map at an arbitrary bias voltage (*i.e.* arbitrary energy).

Here, it should be noted that, though dI/dV at a point is proportional to $N(r, E)$ at the point, the dI/dV map does not always reflect the spatial change in the LDOS because of so-called "set point effect" [16]. Using the equation (2.7), $g(r, z_0, V)$ becomes

$$g(r, z_0, V) = \frac{eI_0 N(r, eV)}{\int_0^{eV_0} N(r, E)dE} \tag{2.9}$$

This formula includes $N(r, eV)$ in both of the numerator and the denominator. In usual metals, $\int_0^{eV_0} N(r, E)dE$ is uniform spatially. Thus, $g(r, z_0, V)$ represents the spatial change in the LDOS. However, in general, $\int_0^{eV_0} N(r, E)dE$ is not necessarily uniform in real space, especially in exotic materials . Therefore, dI/dV conductance is not always proportional to the LDOS. To avoid this difficulty, following maps have been proposed.

Ratio map

One of a method to avoid the "set point effect" is to take a ratio between $g(r, z_0, \pm V)$ or $I(r, z_0, \pm V)$,

$$Z(r, z_0, V) \equiv \frac{g(r, z_0, +V)}{g(r, z_0, -V)} = \frac{N(r, +eV)}{N(r, -eV)} \tag{2.10}$$

$$R(r, z_0, V) \equiv \frac{I(r, z_0, +V)}{I(r, z_0, -V)} = \frac{\int_0^{eV} N(r, E)dE}{\int_{-eV}^{0} N(r, E)dE} \tag{2.11}$$

Although these maps do not give $N(r, eV)$ directly, these maps purely represent the ratio between LDOS at $\pm eV$ or integrated LDOS without "set point effect".

2.4 Experimental setup

In this thesis, all STM/STS measurements were done at 4.2 K to obtain tunneling spectra with less thermal broadening and to minimize the thermal drift. To cool the STM down to 4.2 K, a vacuum can, in which an STM head is placed, with inner pressure of about 1×10^{-7} torr was inserted into a 60 L liquid helium dewar vessel, as shown in Fig. 2.3. Then, pure helium gas of a few torr is introduced into the vacuum can as an exchange gas. The dewar is placed on a vibration isolation stage to avoid vibration noise.

I employed two types of scanning tunneling microscopes. One is the STM in which a stepping motor is used for coarse motion, and another is the STM in which share piezos are used for coarse motion. The STM with the stepping motor is rather conventional in our laboratory, and thus, I call the STM as the standard type STM. The STM with share piezos is invented by S. Pan, and enables one to perform experiments with high stability compared with the standard one [17]. I call the STM as Pan-type STM named after the inventor. I will describe detail in these STMs and several experimental procedures as follow.

2.4.1 Standard-type STM

Left figure in Fig. 2.3 shows a schematic drawing of the standard type STM. An STM head, in which a sample, a tip, a scanner piezo and so on are placed, is put on the bottom of the vacuum can. Coarse approach is done by using a stepping motor on the top flange of the vacuum can. The stepping motor turns a screw in the STM head through the drive shaft about 1.5 m long, and the scanner piezo and the STM tip are approached toward the sample. Because of looseness of mechanical parts, stability of the tunnel junction is not so good, and it makes precise measurements difficult.

Clean surface of the sample is prepared by cleavage *in situ*. For this purpose, a sample stage can be moved one dimensionally in the STM head through another shaft (cam shaft). The sample cleavage was done as shown in Fig. 2.5(a). This motion of the sample stage also enables us to investigate different locations on the sample surface. However, because of the looseness of mechanical parts and thermal flow throughout the cam shaft, the motion of the sample stage prevents one to perform STM/STS measurements which take a long time.

2.4.2 Pan-type STM

Right figure in Fig. 2.3 shows a schematic drawing of the Pan-type STM. In the Pan type STM, the STM head consists of a sample and a prism, in which an STM tip and the piezo scanner are placed. The prism is fixed by six share piezos, as schematically shown in Fig. 2.4. Course approach is done by using the motion of the share piezos in the following process. First, all piezos are discharged (Fig. 2.4(b)). Then, each share piezo is charged rapidly and slips along the prism one by one (Fig. 2.4(c)). During the motion, the prism doesn't move. After all piezos are shared (see Fig. 2.4(d)), they are simultaneously discharged slowly. During this process, the prism is pushed upward (Fig. 2.4(e)). The prism is approached to the sample by repeating the series of the processes. Because share piezos are driven electrically, the drive shaft is absent in this STM (see the right side of Fig. 2.3). The absence of the drive shaft reduces thermal and vibrational noise to the STM head and leads to high stability of the STM.

Furthermore, to avoid the thermal flow through cam shaft for the sample stage slide, the sample is attached to the STM head directly. Sample cleavage was done as shown in Fig. 2.5(b). On a sample stage, which also works to cleave the sample, Au thin film is attached to elucidate the STM tip.

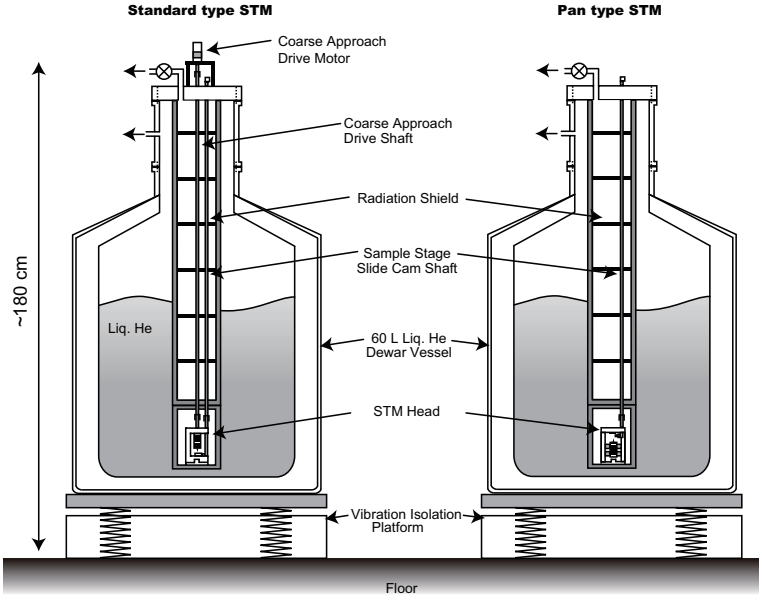

Figure 2.3: Schematic designs of two types of STMs

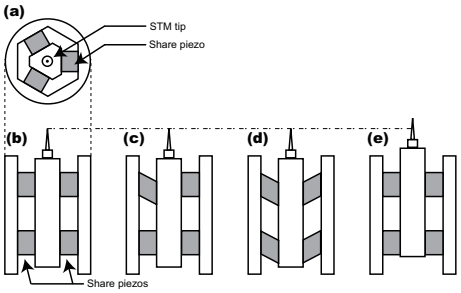

Figure 2.4: Schematic illustrations of the Pan-type STM

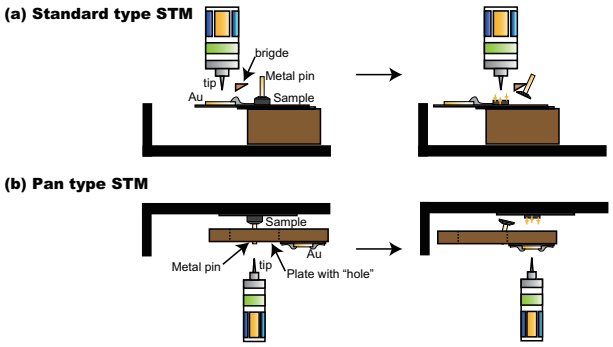

Figure 2.5: Schematic illustrations of preparation of clean surface.

2.4.3 Tip preparation

For the STM/STS measurements, Au wire was used as an STM tip. An Au tip is prepared by electrochemical polishing. Au wire with a diameter of ϕ0.3 and Pt ring, which act as a counter electrode, were soaked into HCl *aq* and DC voltage of 4 V was applied between them. The etching was finished when bubbles are stopped to appear. The etched wire was washed with hot water. The tip was fixed to a tip holder at the end of the piezo tube of the STM head with a silver paste.

Chapter 3

Visualizing the Pt doping effect on surface and electronic states in $Ir_{1-x}Pt_xTe_2$

In this chapter, I will present Pt doping effect on surface and electronic structure in $Ir_{1-x}Pt_xTe_2$ by STM and STS, and discuss the role of Pt dopant.

3.1 Introduction

As described in chapter 1, $IrTe_2$ has the structure composed of stackings of Te-Ir-Te. Each Ir is surrounded by six Te atoms in edge sharing octahedron coordination, as shown in Fig. 1.2 (a)-(c). $IrTe_2$ undergoes a structural phase transition from trigonal to monoclinic (triclinic) structure at the transition temperature T_s of 280 K, and shows abrupt jump in electric resistivity as shown in Fig. 3.4. With chemical doping (such as Pt, Pd, and Rh) at the Ir site, the structural transition is suppressed and superconductivity appears at a transition temperature T_c of 3 K [11, 18, 19]. As in the case of iron-based superconductors, it is expected that an ordered state exists below T_s in $IrTe_2$, and the emergence of superconductivity in doped $IrTe_2$ is related to the disappearance of the ordered state. In fact, below T_s, a periodic SM with a wave vector of $(\frac{1}{5}\frac{2\pi}{a_m}, 0, \frac{1}{5}\frac{2\pi}{c_m})$ is observed by electron, neutron, and X-ray diffractions [20, 21, 25, 26]. Here a_m and c_m are original in-plane and out-of-plane lattice constants. This SM is expected to relate the appearance of superconductivity.

3.1.1 Supermodulation due to partial dimerization

Many experimental and theoretical studies have been done to unveil the nature of the SM, and there are a few possibilities, including the Fermi surface nesting [18], orbitally induced Peierls mechanism [22], reduction of Te 5p electrons [23, 24], and dimerization of Ir 5d electrons [25, 26]. At present, the partial dimerization of Ir ions is most plausible. Local structural change owing to the partial dimerization was revealed by previous XRD study in low temperature [25, 26]. According to the study, dimerized Ir atoms (referred as Ir(3) in Fig. 3.1(a)) are closer to each other. Figure 3.1(b) shows schematic illustration of Ir and Te atoms. Accompanied with the structural change due to dimerization of

Ir atoms, Te atoms which is neighboring dimerized Ir atoms (referred as Te(1) and (5)) are also closer each other. As a result, the octahedron that contains Ir dimer atoms becomes thicker than the others [25, 26]. This is easily understood because the compressed octahedron along the in-plane direction tends to elongate to the horizontal direction. On the other hand, Te atoms which is neighboring non-dimerized Ir atoms (referred as Te(2) to (4)) are separated from each other. [25, 26]. Consequently, the average distance between interlayer (intralayer) Te atoms increase (decrease) [27].

This structural change also modifies electronic states[25, 26]. Theoretical study showed that, at the normal state above 280 K, the DOS derived from Ir t_{2g} electrons is centered at -2 eV below the E_F, and widely distributed across the E_F as shown in Fig. 3.1(c) and (d). There also exists the DOS derived from Te 5p electrons across the E_F, which is strongly hybridized with Ir t_{2g} orbitals. Because of the DOS, $IrTe_2$ shows metallic behavior in resistivity in the normal state. Below the phase transition temperature, the partial dimerization changes the DOS derived from t_{2g} electrons of Ir(3), but the DOS derived from the other Ir electrons dodo not change. For the Ir(3), the t_{2g} DOS splits into two DOS peaks, which are considered as a bonding state and an anti-bonding state, shown in Fig. 3.1(d). Because the bonding state is below the E_F and the anti-bonding state is above the E_F, a large gap opens at the E_F for the dimerized Ir ions. This leads to the reduction of the total DOS at the E_F, and abrupt increase in resistivity and decrease in magnetic susceptibility at the T_s. However, direct evidence for the realization of the partial dimerization has not been obtained yet. This must be investigated by microscopic measurements, such as STS measurements.

3.1.2 Pt substitution effect on $IrTe_2$

Pt substitution effect on the transport properties and the crystal structure were studied by Pyon *et al.*. Pt substitution to Ir site suppresses the T_s, at which abrupt change in resistivity is observed [11]. In $Ir_{0.97}Pt_{0.03}Te_2$, the phase transition is completely suppressed and superconductivity appears at approximately 3 K. Further substitution reduces the T_c. Thus, the electronic phase diagram shows superconducting dome as shown in Fig. 1.7(a), similar to that of superconducting cuprates and iron based superconductors.

Substitution effect on the crystal structure in the normal state is investigated by XRD measurements at room temperature [29]. According to the report, the lattice constant along the a-axis a_0 increases and the lattice constant along the c_0 axis decreases as increasing Pt concentration in the normal phase. Furthermore, the thickness of the Te-Ir-Te layer becomes thin as Pt concentration is increased. The relationship between these structural changes and the suppression of the phase transition by Pt substitution is not clarified. However, Pt substitution seems to prevent Ir ions from dimerization, because the change in a_0 and c_0 by Pt substitution is in an opposite way to the dimerization in $IrTe_2$ [27].

The change in the electronic structure has been investigated by photoemission spectroscopy studies. An ARPES study revealed the chemical potential increases in $Ir_{0.95}Pt_{0.05}Te_2$ by a few meV compared to $IrTe_2$ [30]. Qualitatively, this seems to be valid because Pt^{4+} has one more electron in t_{2g} orbital than Ir^{4+}. Indeed, a band structure calculated for $IrTe_2$ with additional 0.05 electrons per Ir site can reproduce the observed band structure in $Ir_{0.95}Pt_{0.05}Te_2$. Therefore, Pt dopants provide extra carrier to $IrTe_2$ in addition to application of structural change (i.e. increase in a_0 and decrease in c_0) revealed by XRD.

Although the XRD and the ARPES studies revealed the change in crystal structure at room temperature and in the electronic states through Pt substitution, it is still unclear how these changes relate to the suppression of the structural

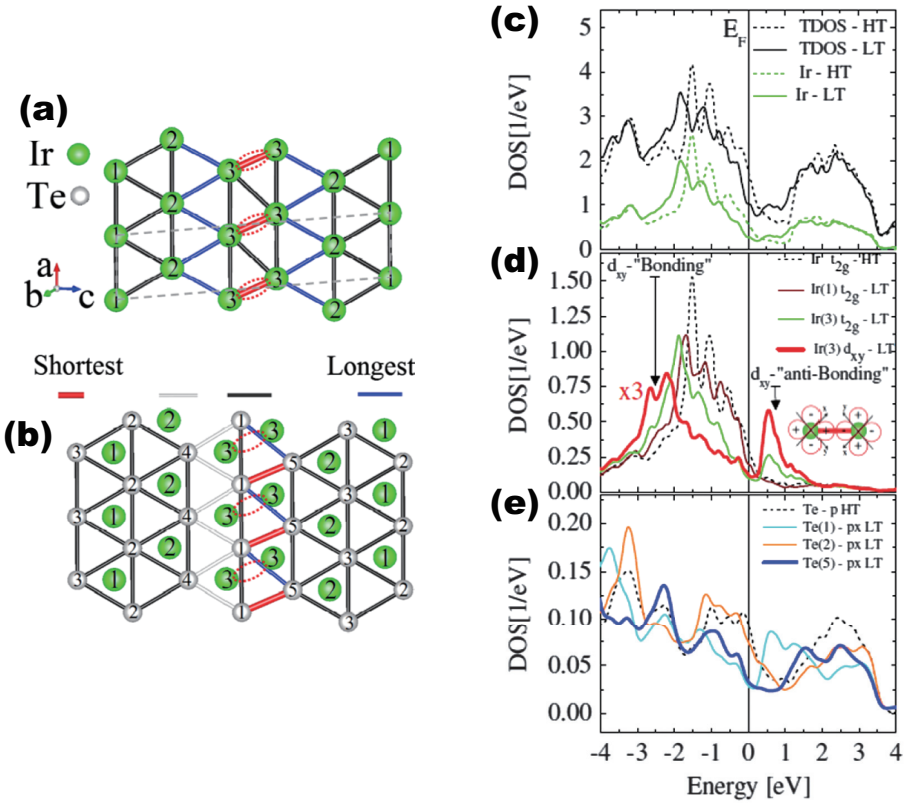

Figure 3.1: Effect of the partial dimerization on the local structure and the LDOS studied by low temperature XRD study and theoretical calculation[25]. (a), (b) difference in the bond length due to the partial dimerization The dimerized Ir ions (referred as Ir(3)) and its neighboring Te ions (referred as Te(1) and Te(5)) are closer to each other. (c), (d), (e) change of the LDOS across the transition.

transition and the emergence of superconductivity. Observation of microscopic change of the SM at low temperature will provide some hints to understand these issues.

3.2 Object of this chapter

As described above, there are some problems to be solved. One is the confirmation of the origin of the SM in $IrTe_2$. Second is the effect of Pt dopant: How the Pt doping suppresses the SM and enhances superconductivity. Clarification of these problems is the object of this chapter. To investigate these problems microscopically, I performed STM/STS measurements in Pt doped $IrTe_2$. In this chapter, I present the results of STM/STS measurements and discuss these problems.

3.3 Sample growth and characterization

3.3.1 Single crystal growth

Single crystals $Ir_{1-x}Pt_xTe_2$ are grown by the self-flux method. The self-flux method is a method where components are dissolve in a flux, which is also a component. In this case, the flux is Te. Ir powder and Pt wire, and Te grain are sealed in a quartz tube in the morr ratio of 0.18(1-x):0.18x:0.82. The sealed quartz tube with raw materials is heated in a furnace with a sequence shown in Fig. 3.2(a) [24]. Single crystals of $Ir_{1-x}Pt_xTe_2$ with x = 0, 0.01, 0.02, 0.04, 0.07 and 0.15 are prepared with the same heating sequence. The obtained single crystals are shown in Fig. 3.2(b).

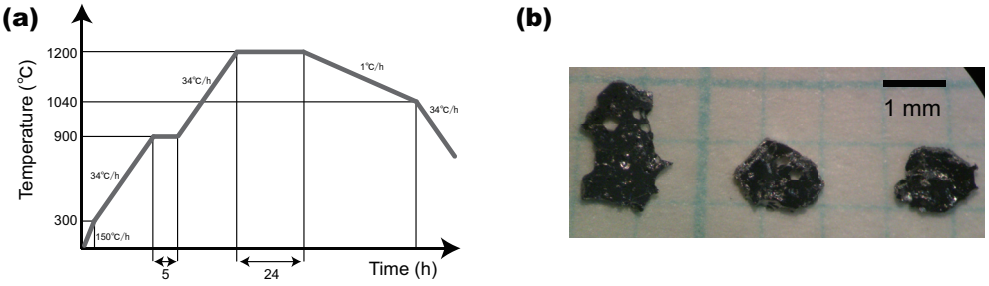

Figure 3.2: (a) Heating sequence for crystal growth of $Ir_{1-x}Pt_xTe_2$. (b) A picture of single crystals of $IrTe_2$.

3.3.2 Characterization of the single crystals

Crystal structure of these samples is evaluated by XRD measurements at room temperature, thus in the normal state. Each single crystal is crashed into powder to obtain diffraction from not only (00l) but also (h,k,l) planes. Figure 3.3(a) shows the XRD results. Almost all diffraction peaks can be assigned to the Mirror indices reported previously [24]. Figure 3.3(b) shows the lattice constant along the a_0 axis and the c_0 axis of different Pt concentrations. These lattice constants are calculated from the diffraction from the (001) and (101) planes. These lattice constants a_0 and c_0 tend to increase and decrease as increasing x, respectively. Furthermore, change in c_0 is larger than that in a_0. These qualitative features are in good agreement with previous XRD results [11, 29].

To evaluate the ground state of each sample, resistivity measurements were done by standard four probe method. Figure 3.4(a) shows the temperature dependence of the resistivity in $Ir_{1-x}Pt_xTe_2$ (x = 0, 0.01, 0.02, 0.04, 0.07 and 0.15). Each of them are normalized at the value at 300 K and shifted upwards by 0.5 for clarity. In the sample with x = 0, 0.01, 0.02, and 0.04, abrupt increase in resistivity is observed at 280, 268, 218, and 212 K, respectively. These indicate that the phase transition is suppressed gradually with increase in Pt concentration. At x = 0.07, the structural transition is completely suppressed and superconductivity appears at 2.8 K (see Fig. 3.4(b)). The sample with x = 0.15 shows neither the structural transition nor the superconducting transition.

T_s and T_c of each sample are summarized in table 3.1. These results are qualitatively consistent with those reported previously [11, 28]. However, the reported Pt concentration at which T_c appears is much lower than our nominal value: In the previous report, the concentration in which superconducting transition is observed at 2.8 K is approximately x =

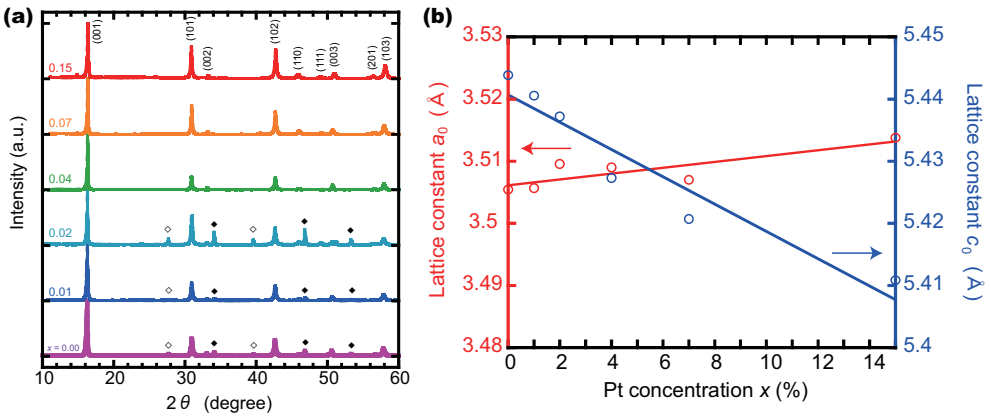

Figure 3.3: (a) XRD results of $Ir_{1-x}Pt_xTe_2$ (x = 0, 0.01, 0.02, 0.04, 0.07, 0.15). Each profile is shifted upward for clarity. Here, peaks denoted by white and black diamonds are due to Te and $Ir_{0.75}Te_2$ impurities, respectively. (b) Lattice constants of $Ir_{1-x}Pt_xTe_2$ (x = 0, 0.01, 0.02, 0.04, 0.07, 0.15) estimated from diffraction from the (001) and the (101) planes.

Nominal concentration of dopant	Concentration of dark spots	T_s (K)	T_c (K)
0.00	0.000	280	-
0.01	no data	268	-
0.02	0.008	218	-
0.04	0.01	212	-
0.07	0.025	-	2.8
0.15	0.073	-	-

Table 3.1: A list of samples used in this study. Concentration of the dark spots is estimated from the STM images shown below. T_s and T_c are estimated from the electric resistivity measurements of each sample.

0.04, while x = 0.07 in our sample. Furthermore, the same T_s appear at much lower concentrations in reported sample than our samples. This indicates that the nominal concentration of our samples is different from actual concentrations. To estimate actual concentrations, I plotted T_s normalized by T_s at x=0 vs Pt concentration as shown in Fig. 3.3(b). The relation between normalized T_s and Pt concentration is linear in both our samples and the reported values, though the slope in our sample is about half. Thus, it is concluded that the actual Pt concentrations in our samples are about a half of the nominal one.

3.3.3 Privious STM/STS measurements in $IrTe_2$

Before the discussion about the change in the surface structure and the electronic states in Pt substituted samples, I present previous STM/STS results of $IrTe_2$ performed by our group at 4.2 K, which is lower temperature than the T_s of 280 K [32]. Figure 3.5(b) shows the STM image in $IrTe_2$. As can be expected, uni-directional atomic modulation is observed. The wave vector of the SM is $(\frac{1}{5}\frac{2\pi}{a_0}, 0)$, and is consistent with previous diffraction studies [20, 21, 25, 26].

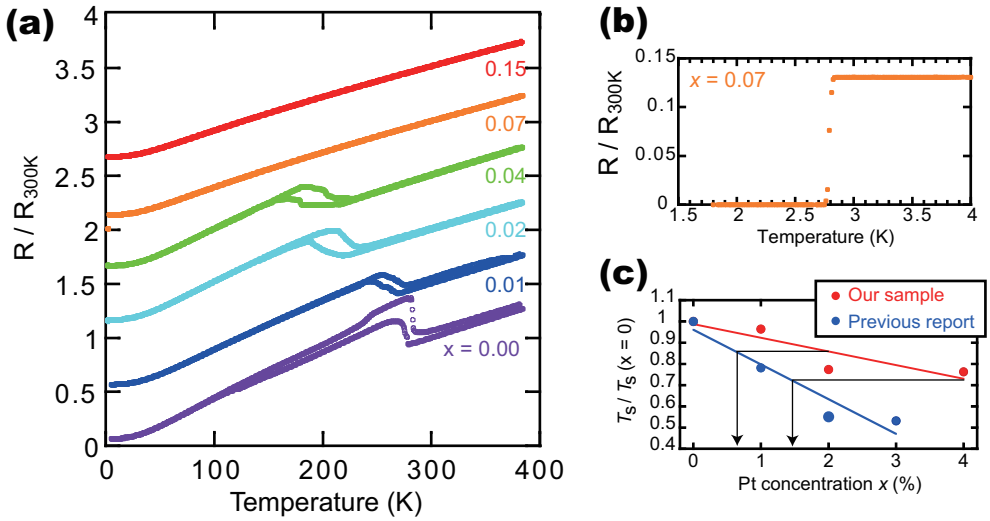

Figure 3.4: (a) Temperature dependence of resistivity in $Ir_{1-x}Pt_xTe_2$ (x = 0, 0.02, 0.04, 0.07, 0.15). Each of them is shifted upwards by 0.5 for clarify. (b) Temperature dependence of resistivity in $Ir_{0.93}Pt_{0.07}Te_2$ from 1.8 to 4 K. The superconducting transition occurs at 2.8 K. (c) Structural transition temperature (T_s) normalized by that of $IrTe_2$, 280 K as a function of nominal Pt concentration x. To estimate the actual concentration of our samples, normalized T_s reported previously is also shown [11].

Figure 3.5(a) shows tunneling spectra taken at the trough and the crest of the SM. There exist several features in the spectra. One is the existence of the finite conductance at 0 mV, which is consistent with the metallic behavior in the electric resistivity. Second is asymmetry with respect to 0 mV. This is also consistent with both of the calculated DOS of Ir and Te [25]. Third is that the spectrum taken at the trough is more asymmetric than at the crest. This can be confirmed from the dI/dV map at -350 mV shown in Fig. 3.5 (c) at the same field of view of the STM image shown in Fig. 3.5(b). Because the dI/dV conductance below -200 mV in the trough is larger than in the crest, the trough has high intensity in the dI/dV map. Here, it is noted that the difference in the conductance below -200 mV is not necessary to be considered as the difference in the LDOS at 200 meV below the E_F, because of the set point effect described in chapter 2. Thus, we focus on the difference in the asymmetry in each spectrum taken at the crest and the trough of the SM.

According to the theoretical calculation shown in Fig. 3.1(e) [25], the asymmetry in the LDOS around E_F varies depending on the site: at the Te sites above the dimerized Ir atoms (refered as Te(1) and (5)), the LDOS shows less asymmetry than that at the other Te sites. Thus, the observed change in the asymmetry in the LDOS is thought to be due to the partial dimerization of Ir atoms. If the expectation is valid, we can identify that Te atoms on the crest of the SM, where LDOS is less asymmetric, correspond to Te(1) or (5). The fact that the Te(1) and Te(5) exist in the crest is consistent with low temperature diffraction studies [25, 26].

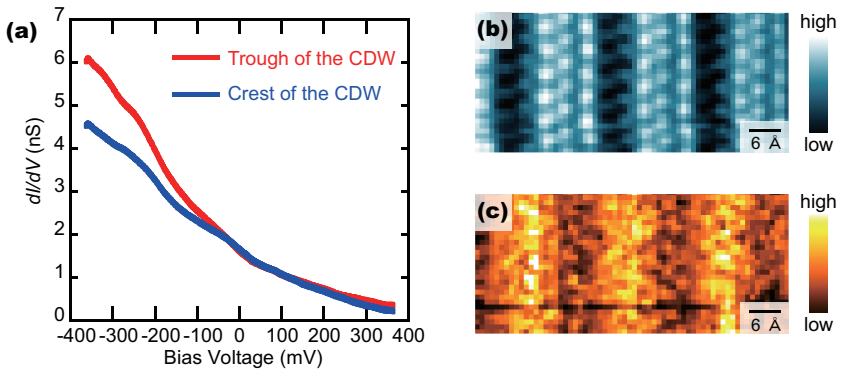

Figure 3.5: Surface and electronic structure of $IrTe_2$. (a) Typical tunneling spectra of $IrTe_2$. (b), (c) An STM image with atomic resolution and the corresponding dI/dV map taken at -350 mV.

3.4 Results and discussion

In this section, I will describe STM/STS results of $Ir_{1-x}Pt_xTe_2$. All measurements were performed at 4.2 K, which is higher temperature than the maximum T_c in $Ir_{1-x}Pt_xTe_2$. Thus, all results were obtained in non-superconducting state.

3.4.1 Doping evolution of the surface structure

I observed doping evolution of the surface structure. Figures 3.6(a)-(e) show typical STM images of the samples with nominal x = 0, 0.02, 0.04, 0.07, and 0.15, respectively. In all images, a triangular lattice composed of top-most Te atoms can be seen. Furthermore, different superstructures are superimposed to the triangular lattice of Te atoms on each sample.

In the samples with x = 0.02 and 0.04, the SM with the same modulation wave vector as that of $IrTe_2$ is observed. Thus, the period of the SM doesn't change despite the different Pt concentration. Because Pt substitution increases the carrier number as reported by ARPES measurements [30], this leads the increase in the E_F, resulting change in the Fermi surface nesting wave vector. Thus, if the SM in this material is owing to the Fermi surface nesting, the wave vector of the SM must be changed with increasing Pt concentration. This is disagree with the observed results shown in 3.6(a)-(c), indicating that the SM in this material is not due to the Fermi surface nesting. This fact supports the scenario of the partial dimerization as origin of the SM.

Figure 3.6(d) shows an STM image of the sample with x = 0.07, which shows superconductivity below 2.8 K. I found that the surface is randomly paved with patches with an area of a few nm^2. In the followings, I will call this superstructure as the "patchwork structure (PS)". The size of the patches is rather random. The boundary of each patch tends to be parallel to the atomic lattice of Te.

The coexistence of the SM and the PS was seen in a part of the sample, which is perhaps due to the non-uniform distribution of the dopant. An example in a sample with x = 0.02 is shown in Fig. 3.5(g). The change in the surface from the SM to the PS is rather abrupt and we have not observed other types of surface structure, such as the SM with a different modulation period. The size of the patch observed in such a region is larger than that observed in

$Ir_{0.93}Pt_{0.07}Te_2$ shown in Fig. 3.5(d).

The PS disappears on the 15% Pt doped sample. Thus, the PS appears only in the superconducting sample. From the observations, the PS seems to correspond to the appearance of superconductivity.

In all Pt substituted samples, several black contrasted spots can be seen. Because these contrasted spots can be seen in Pt substituted samples only, it seems that the contrasted spots correspond to Pt substituted sites. Because of the lack of the SM or the PS, the detail of the contrasted spots can be observed in Fig. 3.6(e). The STM image in Fig. 3.6(e) shows that the black contrasted spots spread over the neighboring three Te atoms. As can be seen in the magnified image in Fig. 3.7(a), the center of the three Te atoms is darkest. This darkest position can be an Ir site underlying the top-most Te layer (I refer the site as the A site) or Te site underlying the Ir layer (I refer the site as the B site), as shown in Fig. 3.7(b). One cannot distinguish two site from STM measurements on the surface because both sites locate at the center of neighboring three Te atoms in the STM image. However, all black spots are connected by linear combination of the in-plane unit vector. This indicates that all the spots are located in either A or B site.

Similar black spots to those in Fig. 3.6(e) can be seen in the other samples with different Pt concentrations. I found that the number of the black spots is different in different doping samples. Figure 3.7(c) shows the number of the dark spots in each sample as a function of the nominal Pt concentration. The figure clearly represents that the number of the contrasted spots is proportional to the nominal Pt concentration. Because all the contrasted spots can be A site, it is plausible that each darkest position shown in Fig. 3.7(a) corresponds to the Pt sites which is substituted in Ir sites. Note that the concentrations of the dark spots are less than the nominal dopant concentrations. This is because, as we mentioned, the actual concentrations in our samples are less than the nominal ones as expected from the results of the resistivity measurements.

Figures 3.5(h)-(j) show the cross-sectional profiles indicated by white line shown in Fig. 3.5(d), (e), and (h), respectively. These indicate height variations in STM images due to the SM, the boundary of patches, and the dopant. As can be seen from these profiles, the height variation of both the SM and the boundary of patches is about 0.1nm. On the other hand, the variation due to the dopant is about 0.02 nm.

In general, STM images reflect both surface geometry and local electronic states as presented in chapter 1. However, the observed contrast or cross sectional profiles in Fig. 3.6 can be explained by surface geometry only, as follows. XRD measurements at room temperature determined that the layer thickness of $IrTe_2$ and $Ir_{0.93}Pt_{0.07}Te_2$ is 0.2733 nm and 0.2722 nm, respectively [29]. Because STM measurements determined that the reduced local height due to Pt doping is 0.02nm, if we assume that this value is purely geometrical one, the layer thickness of $PtTe_2$ is expected to be 0.2733-0.02 $\times$ 2 = 0.2333 nm. The factor 2 is for the both side of the layer. Then, assuming that the layer thickness is the average of the height of $IrTe_6$ and $PtTe_6$ octahedrons with a ratio of 1:1-x, the actual Pt concentration x is estimated to be approximately 0.03 from

$$0.2733 \times (1 - x) + 0.2333 \times x = 0.2722 \tag{3.1}$$

This value is in good agreement with that estimated from the resistivity measurements and the concentration of the Pt dopants in the STM images. Thus, this indicates that local height reduction near Pt site observed by STM measurements shown in Fig. 3.6(e), (i), and 3.7(a) is purely geometrical one induced by the atomic displacement.

3.4.2 Electronic structure near Pt site and patchwork structure

Next, I investigated the electronic states near a Pt site and the PS. First is the electronic states near Pt site. Because Pt site can be observed at any Pt doped samples, the electronic states near Pt site can be measured on any $Ir_{1-x}Pt_xTe_2$ samples. However, as described in 3.4.3, the LDOS is modulated by the SM. Thus, such a structure makes the interpretation of the change in the LDOS due to the Pt dopant difficult. To reduce such an effect, I performed STS near the Pt site on a rather flat surface, namely, on a large patch of $x = 0.07$ sample. Fig. 3.8(a) shows a STM image of a Pt site on a patch. As indicated by blue and purple circles, the triangular lattice of Te atoms and the depression due to dopant Pt can be seen clearly. Figure 3.8(c) shows tunneling spectra. One is the averaged spectrum on the three Te sites which surround the Pt site, and the other is the averages spectrum on the other Te sites. Both spectra show similar features to those observed in $IrTe_2$, *i.e.* finite conductance at 0 mV and asymmetry with respect to 0 mV. The difference between them is their asymmetry as in the case of the SM in $IrTe_2$: The spectrum near the Pt site is more asymmetric than that on the other Te atoms. The difference is conspicuous below -100mV.

The asymmetry in the spectra is also seen in R map at 350 mV defined as

$$R(\mathbf{r}, 350\text{mV}) = I(\mathbf{r}, -350\text{mV})/I(\mathbf{r}, +350\text{mV}) \tag{3.2}$$

, as shown in Fig. 3.8(b) [1]. As can be seen from the R map, the black contrasted region, where the spectrum has larger asymmetry, corresponds to the region where the STM image shows black contrast.

Next, I will discuss about the electronic states in the PS appeared on the sample which shows superconductivity. As shown in the previous section, the PS consists of patches randomly paved. In the following, I call a terrace on a patch as a crest, and a wall between patches as a trough. Figure 3.9(b) shows the tunneling spectra taken at the crest and the trough on the PS shown in fig. 3.9(c). Both spectra have finite conductance at 0 mV and are asymmetric with respect to 0 mV. Furthermore, the spectrum at the trough is more asymmetry than at the crest. This tendency also can be confirmed in a conductance map taken at -350 mV, where the trough shows higher intensity than the crest. These results indicate that the crest and the trough of the PS have almost same electronic features as those in the SM in $IrTe_2$ shown in Fig. 3.9(a) in this energy range. This is consistent with the results in ARPES where almost no difference exists in the electronic structures near E_F between $IrTe_2$ and Pt substituted $IrTe_2$ except the shift of the E_F [30].

3.4.3 Discussion

As shown above, I observed the Pt doping evolution of the surface structure and the spatial change of the asymmetry in tunneling spectra. First, I discuss the origin of the difference in the asymmetry of tunneling spectra. The almost same asymmetry of tunneling spectra was observed in the SM, the PS and near the doped Pt sites. As shown in the previous section, the observed contrast in the STM images mainly comes from the surface geometry. Because the change in the asymmetry of tunneling spectra corresponds to the STM contrast, it is thought the origin of the change in the spectra is the change in the surface height, *i.e.* the displacement of atoms, such as local deformation of $IrTe_6$ (or $PtTe_6$) octahedrons, which affects the electronic states of Te $5p$ electrons. Thus, the change in the electronic states of

[1] The R map purely represents the ratio to integrated LDOS from -350 meV to 0 meV and from 0 meV to 350 mV, without "set point effect" as described in chapter 1.

Te 5p electrons seems to be responsible for the change in the asymmetry in tunneling spectra.

Next, I discuss the formation of the PS. Since the differences of the electronic states and the height between the trough and the crest in the SM are almost same as those in the PS, the PS can be understood as the disordered SM. As shown in the previous section, the SM in $IrTe_2$ is understood with chemical bonding picture, i.e. partial dimerization. Furthermore, the observed walls in the PS are almost along the three directions which are equivalent because of three fold symmetry of the crystal. Thus, the PS is thought to be also caused by partial dimerization. Since the doped Pt induces local suppression of height as is caused by the dimerization, it is plausible that the local suppression of height by Pt doping caused the random distribution of dimerized regions, resulting the PS. This is supported by the fact that the size of the observed patches in the PS depends on the concentration of doped Pt as shown in Fig. 3.6(g). Thus, further doping of Pt decreases the residual dimers, resulting the surface without any superstructure.

Finally, I discuss the relation between the observed PS and the appearance of the superconductivity. As for the origin of the superconductivity of this material, the structural fluctuations which relate to Ir orbital has been proposed [11]. In our experiments, we found that the PS was observed in the samples which show superconductivity, and the PS was composed of random distribution of dimerized regions. The destruction of the aligned dimer rows and the appearance dimer rows with short coherence length are thought to increase the structural fluctuation of Ir-Ir bond. Thus, the appearance of the PS indicates the enhancement of the structural fluctuations. This is consistent with the proposed origin of the superconductivity.

3.5 Summary

STM/STS measurements were performed in Pt substituted $IrTe_2$. STM observations revealed different surface structures depending on the ground states. Pt concentration independent period of the SM suggests that the SM is not due to Fermi surface nesting, but dimerization. The emergence of the PS is due to the local deformation of the octahedrons caused by substituted dopants. The change in the asymmetry of tunneling spectra is due to the local deformation of MTe_6 (M: Ir or Pt) octahedrons. The appearance of the superconductivity is thought to relate the increase in the structural fluctuations due to the appearance of the PS. Thus, providing the local structural stress seems to be a primary role of the substituted Pt for the suppression of the SM and emergence of superconductivity.

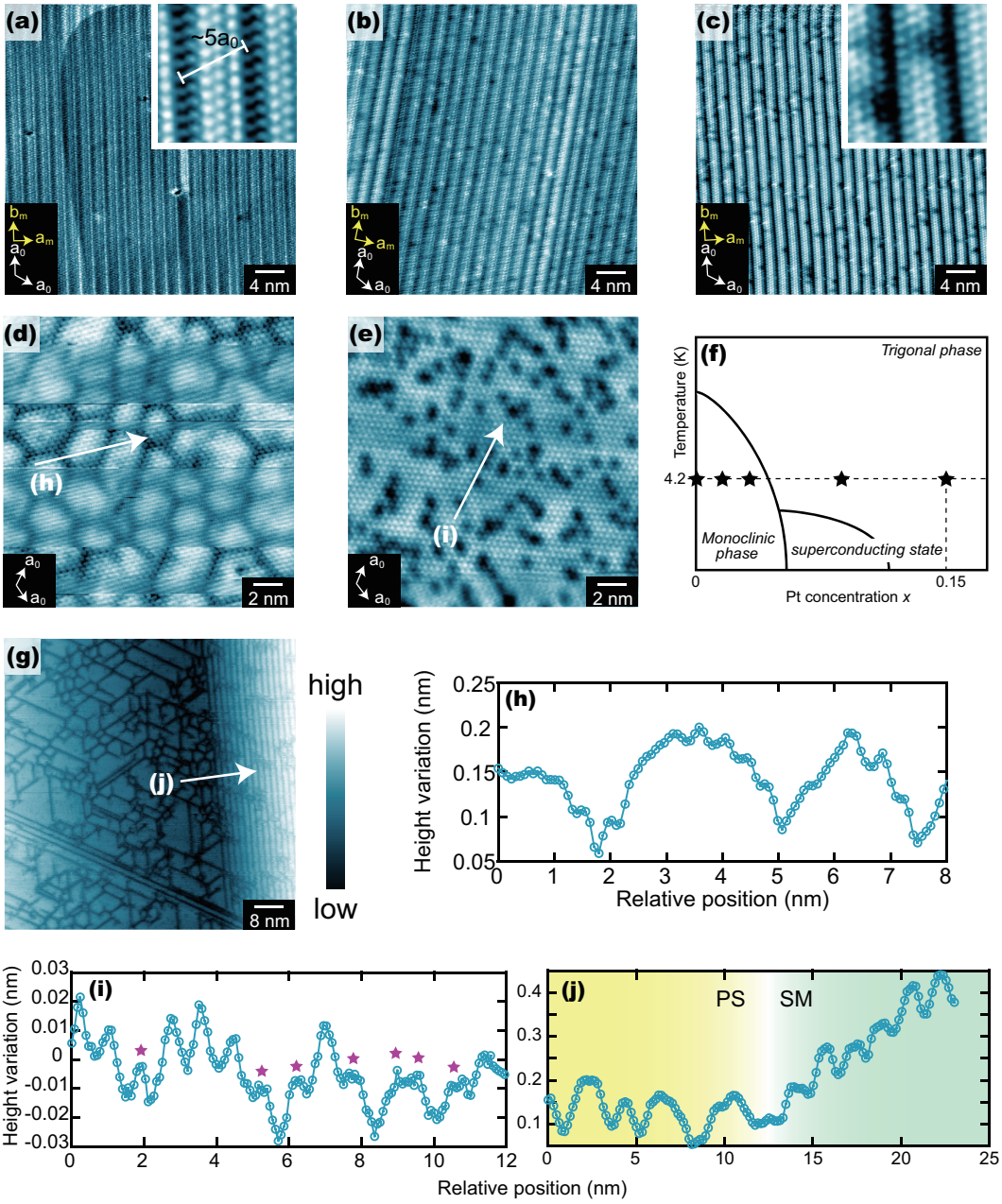

Figure 3.6: Doping dependence of the STM images. (a)-(e); Typical STM images of the sample with $x = 0$, 0.02, 0.04, 0.07, 0.15, respectively. Inset figures of (a) and (c) represent the magnified STM images, which show a triangular lattice of Te atoms and the SM. (f); Schematic phase diagram of Pt doped $IrTe_2$. Each star represents the Pt concentration where I performed STM measurements. (g); An STM image which shows the coexistence of the SM and the PS. (h); STM line profile of the PS along white line in (d). (i); STM line profile across the Pt site along the white line in (e). Purple stars indicates the Te atoms that are depressed by dopant Pt. (j); STM line profile along the white line in (g). The height variation of each patch is almost same order as the amplitude of the SM.

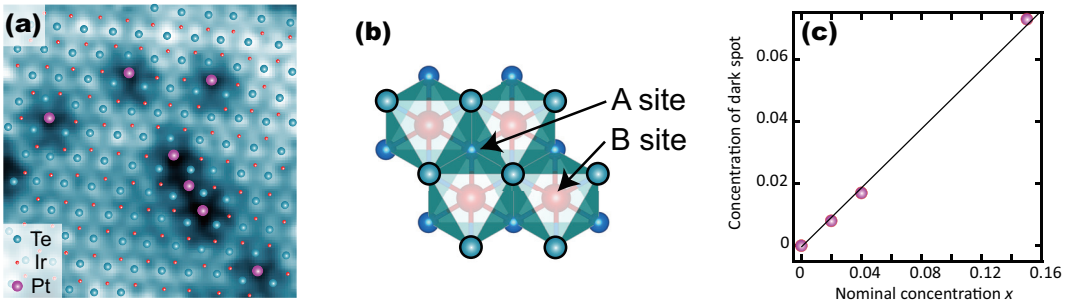

Figure 3.7: (a) Magnified STM image of the sample with $x = 0.15$. (b) Two possible sites where the black contrasted region is observed in the STM image (a). (c) Concentration of the black contrasted region as a function of nominal Pt concentration x.

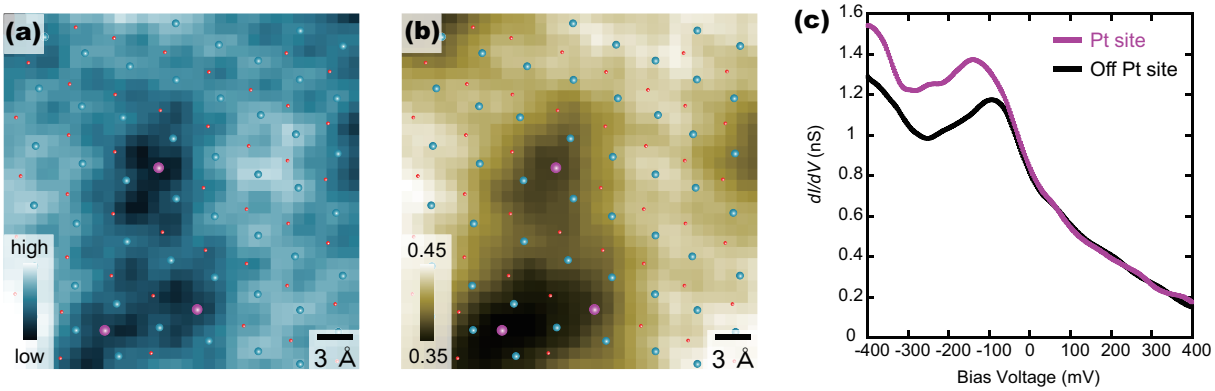

Figure 3.8: The electronic states of the Pt site. (a) An STM image that contains the three Pt site. (b) The corresponding current ratio map taken at 350 mV. See the text for more detail about the map. (c) Tunneling spectra taken on and off the Pt site. The set point is 500 mV/500 pA.

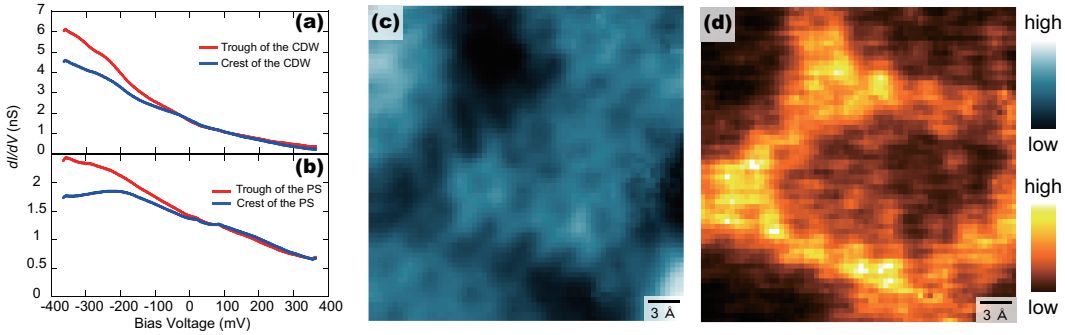

Figure 3.9: STS results on the patchwork structure. (a); Tunneling spectra taken at the crest and the trough of the SM in pristine $IrTe_2$. (b); Tunneling spectra taken at the crest and the trough of the SM in pristine $IrTe_2$. (c), (d); An STM image and corresponding dI/dV conductance map at -350 mV. The set point of each data is 300 mV/300 pA for (a), 500 mV/500 pA for (b), 500 mV/500 pA for (c) and (d).

Chapter 4

Effect of Fe substitution on surface and electronic states in $Ta_{1-x}Fe_xS_2$

In this chapter, I will show the results of scanning tunneling microscopy and spectroscopy measurements on iron doped $1T$-$Ta_{1-x}Fe_xS_2$.

4.1 Introduction

$1T$-TaS_2 is one of the most studied TMDC, because of the existence of several CDW states. Furthermore, this material shows the Mott state. Mott physics has attracted much attention because it provides a stage of exotic electronic states. Exotic electronic states usually appear when a Mott state melts into a metallic state. For example, in cuprates, high temperature superconductivity appears when the Mott state is melted by carrier doping. Thus, the melting of the Mott state is an important problem in Mott physics. Recently, it was found that the Mott state in $1T$-TaS_2 melts into a metallic state with several techniques. In addition, superconductivity was found to emerge when the Mott state melts into the metallic state as shown in chapter 1. Furthermore, the appearance of a spatial pattern has been discussed when the Mott phase melts, as described below. Thus, it is interesting to investigate how the spatial pattern evolves with melting in real space.

In this section, I will describe basic properties of $1T$-TaS_2 and summarize recent studies related to the melting of the Mott state.

4.1.1 CDW states of $1T$-TaS_2

$1T$-TaS_2 undergoes successive CDW transitions at 600, 350, and 180 K. Below 180 K, it is in a commensurate CDW (CCDW) state. In this state, so called 'David-star' cluster composed of 13 Ta atoms forms a triangular lattice, as shown in the inset figure of Fig. 4.2(a). The periodicity of the CCDW a_{CCDW} is $\sqrt{13}a_0 = 3.61a_0$, and its direction is rotated by 13.5 degree with respect to that of the unit cell vector, as shown in Fig. 4.2(a). This phase is the Mott phase, which

originates from strong correlation effect between Ta 5*d* electrons located at the center of each David-star [34]. In this state, electric resistivity shows insulating behavior.

The Mott insulating state is characterized by the electrons that are localized at the center of each David-star. The localized electrons form shallow bands below and above the E_{F}. These two bands are called the lower and upper Hubbard bands (LHB and UHB) respectively, and result in a Mott gap at the E_{F}. The Mott gap can be observed by STS. Figure 4.1(a) and (b) show tunneling spectra taken at the crest and the trough of the David-stars in the Mott state. As a common feature, tunneling conductance at 0 mV is almost zero, consistent with the insulating behavior of the electric resistivity in the Mott phase. In addition, there exist two peaks at approximately -300 mV and +200 mV. These peaks are derived from the UHB and LHB, respectively. Thus, the Mott gap was estimated to be approximately 500 meV. The difference in tunneling spectra between crests and troughs can be seen in the intensity of the LHB and the UHB peaks; the peaks at the crest are enhanced compared to that of the trough. This is because the electrons which form the UHB and LHB are localized at the center of David-stars.

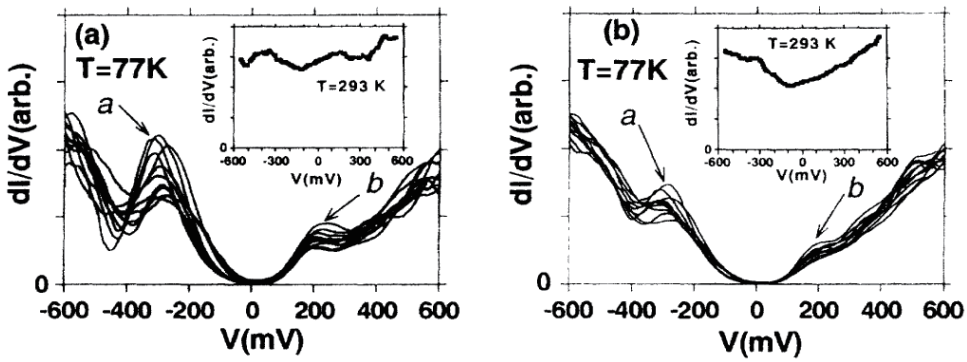

Figure 4.1: Electronic structure of TaS_2 revealed by STS measurements [34]. (a) Tunneling spectra taken at the crest of the David-stars. (b) Tunneling spectra taken at the trough of the David-stars. The peak structures corresponding to the LHB and the UHB are enhanced at the crest, because the corresponding electrons are localized at the crest.

When temperature is increased from the CCDW state, a nearly commensurate CDW (NCCDW) state emerges. In the NCCDW state, the spatially uniform CCDW is divided into hexagonal domains by domain walls called discommensurations, as shown in Fig. 4.2(b) [35]. At the same time, accompanied with the structural change, the Mott insulating state melts into a metallic one.

When temperature is further increased, it undergoes the successive phase transitions from the NCCDW state to an incommensurate CDW (ICCDW) and a normal state at 350 and 600K, respectively[33].

4.1.2 Melting of the Mott state in 1T-TaS_2

The melting of the Mott state in 1T-TaS_2 is not only caused by the increase in temperature. Sipos *et al*. reported that application of hydrostatic pressure suppressed the Mott state. Furthermore, superconductivity was found to emerge up to high hydrostatic pressure. Thus, the melting of the Mott state in 1T-TaS_2 realizes superconductivity. They argued the appearance of a textured CDW state, which consists of metallic interdomain spaces and CCDW domains when the Mott

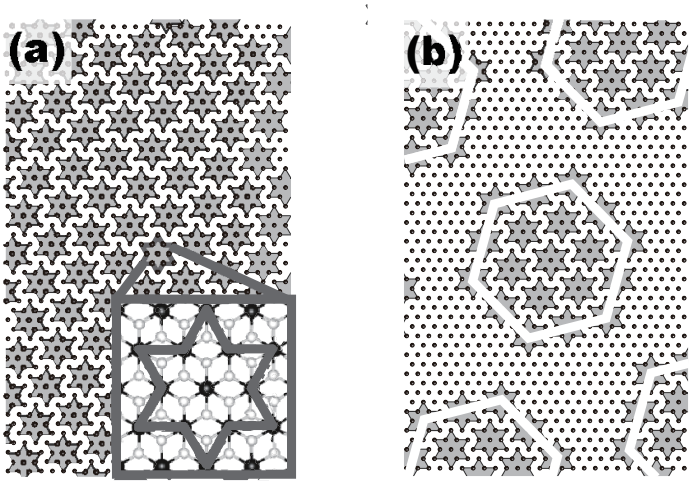

Figure 4.2: Schematics of the CDW formations in TaS_2. (a) the commensurate CDW state and (b) the nearly commensurate CDW state.

state melts. Substitution of constituent elements also suppresses the Mott state, and induces superconductivity. Only substitution of a few percent of Fe was reported to reduce the Mott state and cause superconductivity as described in the next subsection. Substitution of anion also causes the melting of the Mott state and the appearance of superconductivity [49].

Strong external perturbations also melt the Mott state. One is an application of the short pulse laser in the Mott phase, which realized a metallic state with the reduced resistivity [39, 40]. Although the resultant resistivity shows similar value to that in the metallic NCCDW state, comparison study of the transient reflectivity in the melted state and the metallic NCCDW state revealed that they are quite different state. Because of the difference, the melted state is distinguished from the metallic NCCDW state and is called as a "hidden" state. In the hidden state, it is thought that the melting of the Mott state accompanies a spatial pattern caused by the change in the CDW state.

As these reports show, it is thought that the melting of the Mott state in 1T-TaS_2 accompanies a spatial pattern caused by the change in the CDW state. Thus, it is interesting to investigate how the spatial pattern evolves with melting in real space. Recently, an application of a short voltage pulse from a tip of a scanning tunneling microscope was reported to realize a metallic metastable state. The metallic metastable state is accompanied by an anomalous domain structure called the "metallic mosaic" [41, 42]. How this spatial pattern observed in the metastable state relates to the one at the melting of the Mott state by the other techniques such as Fe substitution is an interesting problem.

4.1.3 Fe substitution effect on 1T-TaS_2

The effect of Fe substitution to Ta site is reported by L. J. Li *et al* [12]. Only a slight amount of Fe doping drastically changes the ground state in 1T-TaS_2 as shown in Fig. 1.7(b). Only 1% doping of Fe suppresses the Mott transition

completely, and the sample becomes metallic. When 2% of Ta is substituted by Fe, superconductivity emerges at about 3K. Further Fe substitution reduces the superconducting transition temperature, and the electrical resistivity shows insulating behavior. This is thought to be caused by the Anderson localization [44]. These results are summarized in the phase diagram shown in Fig. 1.7(b) [12]. This phase diagram indicates that the melting of the Mott state is closely related to the emergence of the superconductivity.

Doping dependence of the band structure was investigated by ARPES [43]. According to the study, the band dispersion in the normal state doesn't change with increasing Fe concentration. This suggests Fe dopants provide almost no extra carrier. Furthermore, an electron like band around Γ point in k space is found 100 meV below the E_F at low temperature. Because no other band acrosses the E_F, the authers claimed that this electron band should responsible for the emergence of superconductivity. They also claimed that the real space coexistence of the CDW and superconductivity in Fe substituted 1T-TaS_2.

4.2 Object of this chapter

As described above, the Mott state in 1T-TaS_2 melts into the metallic state and the superconductivity emerges. Furthermore, appearance of spatial pattern such as "hidden state" is expected at the melting of the Mott state. Thus, it is interesting to observe how the Mott state melts in real space, and to investigate the relation between the spatial pattern and the superconductivity. I focus on the Fe doped samples, because of the accessibility by STM/STS. The object of this chapter is to clarify the melting of the Mott phase in Fe doped TaS_2 in real space by STM/STS.

4.3 Sample growth and characterization

4.3.1 Single crystal growth

Single crystals were grown by the chemical vapor transport method. First, we synthesized polyclystal. For the polycrystal growth of $Ta_{1-x}Fe_xS_2$, powder Ta, Fe and S were sealed in a quartz tube in the morr ratio of (1-x) : x : 2.1. It is noted that the excess S was included to obtain 1T polytype. We synthesized samples with nominal concentration x of 0, 0.01, 0.02, 0.03, 0.04 and 0.05. The sealed elements were heated in a furnace with a sequence shown in Fig. 4.3. After the thermal cycle, heated quartz tube was quench into ice water to obtain 1T polytype. Secondly, obtained polycrystal and iodine (5 mg/cc) as a vapor agent was sealed in another quartz tube. Length of the quartz tube was in range of 15 to 20 cm. The tube was heated in a horizontal furnace with the temperature gradient from 950 to 850 Celsius degree. After heating for about a week, the tube was also quenched into a cold water. The obtained single crystals of 1T-TaS_2 are shown in Fig. 4.3(b). The single crystals are gold gray, and mirror-like plates.

4.3.2 Characterization of the single crystals

Crystal structure and electric property of each sample were evaluated by XRD and resistivity measurements, respectively. Figure 4.4(a) shows XRD profiles of single crystals. In all samples, clear (00l) peaks were observed, which indicates that we succeeded in single crystal growth. Figure 4.4 (b) shows the lattice constant along the c-axis, c, of

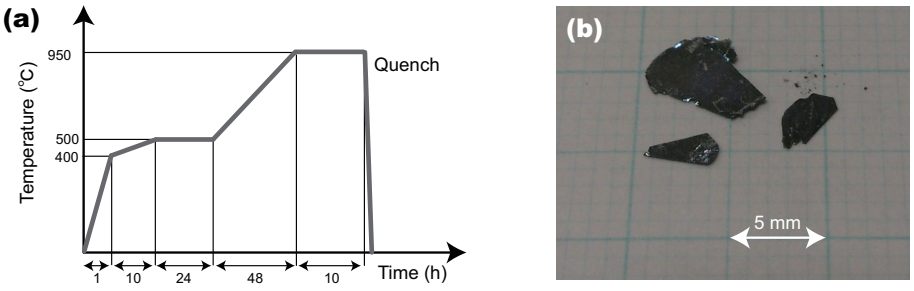

Figure 4.3: (a) Heating sequence for polycrystal growth of $Ta_{1-x}Fe_xS_2$. (b) A picture of obtained single crystal

these samples. c decreases monotonically as increasing Fe concentration. This seems to be due to the difference in the ionic radius between Ta and Fe ions, and is same tendency as that reported previously [12]. Figure 4.4(c) shows the temperature dependence of the resistivity of the single crystals. For the sample with $x = 0$, abrupt increase in resistivity is seen at 180 K for cooling process, which indicates the phase transition to the Mott state. On the contrary, no Mott transition is seen in Fe doped samples. For the sample with $x = 0.01$ and 0.02, decrease in resistivity is observed at low temperature (see the inset figure), indicating the superconducting transition. For the sample above $x = 0.03$, increase in resistivity is seen at low temperature. This behavior is believed to be owing to the Anderson localization as reported previously [44]. These results shown in Fig. 4.4 are consistent with previous report [12].

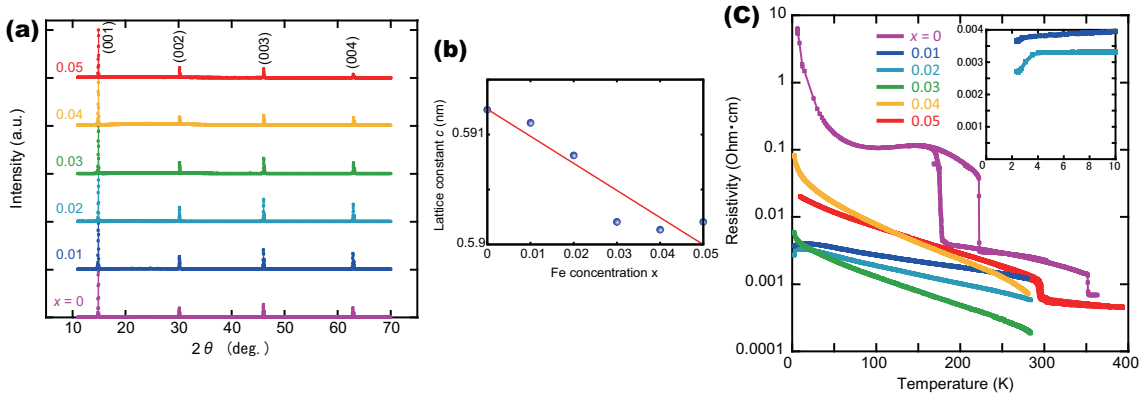

Figure 4.4: (a) XRD profiles of single crystals of $Ta_{1-x}Fe_xS_2$. (b) Doping dependence of the lattice constant c. (b) Temperature dependence of resistivity of each samples.

4.4 Results and discussion

I present STM/STS results of $Ta_{1-x}Fe_xS_2$ observed at 4.2 K in this section. It is noted that 4.2 K is higher than T_c of $Ta_{0.98}Fe_{0.02}S_2$. Thus, all data presented here are results in non-superconducting phase. First, I will show the doping dependence of the surface structures. An anomalous domain structure was observed on the surface of $Ta_{0.99}Fe_{0.01}S_2$.

Next, the evolution of the electronic states with Fe doping will be presented.

4.4.1 Doping evolution of the surface structure of $Ta_{1-x}Fe_xS_2$

The main panels of Fig. 4.5 shows doping evolution of the surface structure of samples with x = 0, 0.01, 0.02 and 0.05, respectively. As shown in the inset of Fig. 4.5(d), surface S atoms modulate and form the David-stars, and an array of the David-stars covers all the surface. These STM images indicate that the David-star itself is stable against Fe doping even at x = 0.05, which is consistent with a previous STM study of Fe doped TaS_2 at room temperature [45]. In all samples, including x = 0, several vacancies can be seen as black points. Although the concentration of the vacancy slightly increases as increasing Fe concentration, the number of the defects is much lower than x. Thus, these vacancies are not thought to be responsible for the site where Fe is substituted, but are thought to be responsible for those of constituent elements.

The STM image at x = 0 where the sample is in the CCDW state shows a triangle regular array of the David-stars. However, Fe doping changes its configuration as follows. When 1% Fe is substituted, the regular array is divided into domains by domain walls. The size of domains is approximately 100 nm^2. The domain walls show white contrast in the STM image taken at a positive bias voltage. The magnified image is shown in the inset of Fig. 2(b). The wall is composed of a one dimensional array of two David-stars, which are closer to each other than in the domain. Because of this change, the phase of CDW, *i.e.*, the phase of the array of David-stars changes across the domain wall. The NCCDW state in pure $1T$-TaS_2 shows periodic domains of the CCDW divided by domain walls. Each domain wall shows dark contrast compared to the commensurate domains in the STM image obtained with a positive bias voltage[35]. In contrast, the domain structure obtained at x = 0.01 shows irregular domains. Furthermore, the domain walls show bright contrast compared with domains. This indicates that the observed domain structure is quite different from that in the NCCDW state from both the structural and electronic points of view.

At x = 0.02, there exist discrete domain walls and white contrasted David-stars. Because the sample at this concentration shows superconductivity, the topographic change must be related to the emergence of superconductivity. We will discuss its relationship with superconductivity later. At x = 0.05, the array of David-stars is so distorted that the domain walls at which the phase change of the array is well defined no longer exist as shown in Fig. 2(d). Such a distortion seems to result in logarithmical increase in resistivity behavior [44].

4.4.2 Spatial evolution of electronic structure of $Ta_{1-x}Fe_xS_2$

As shown in previous section, the surface of the samples shows several features with Fe doping. In this section, I will show the spatial evolution of the electronic states of each sample.

STS results in the sample with x=0.01

As shown in Fig. 4.5(b), $Ta_{0.99}Fe_{0.01}S_2$ showed the domain structure. Figure 4.6(a) and (b) show an STM image of a domain and the corresponding dI/dV map at -100 mV in $Ta_{0.99}Fe_{0.01}S_2$. In the dI/dV map, dI/dV contrast is clearly different between the domains and the domain walls. This indicates the difference in the electronic states between the domains and the walls.

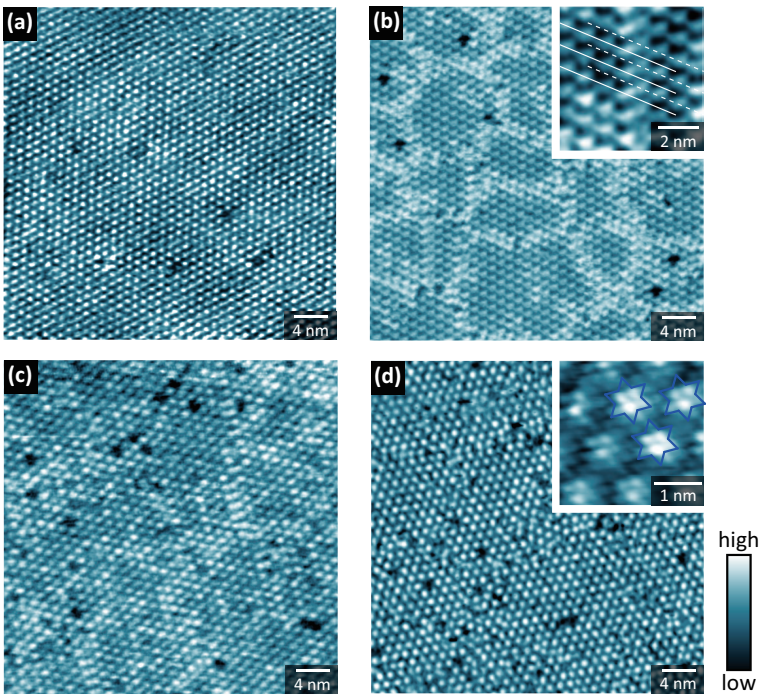

Figure 4.5: STM images of $Ta_{1-x}Fe_xS_2$ (x = 0, 0.01, 0.02, 0.05) in a 50×50 nm^2 field of view. Set point of all images is 500 mV/200 pA. The inset figure of (b) shows a magnified STM image of the domain wall. The inset figure of (d) shows a magnified STM image with atomic resolution.

Typical tunneling spectrum taken at the David-stars in the domain is shown in Fig. 4.6(c). The tunneling spectrum taken at the domain shows two peaks at approximately -150 mV and +100 mV, which may be a reminiscent of the Mott gap. Figure 4.6(d) shows the tunneling spectra along the arrow in the domain shown in Fig. 4.6(a) and (b). The conductance is shown in color scale. The lower graph represents the line profile of the STM image along the line, where each maximum indicate the top of David-stars. The conductance peaks are found to modulate along the row of the David-star with the same period as the David-stars, and show maxima at the top of the David-stars. This behavior is quite similar to that observed in the Mott state in TaS_2 as shown in Fig. 4.1. Thus, the electronic state in the domain seems to have localized nature. However, the electronic state in the domain is different from the Mott state in TaS_2 in several points of view. One is the finite DOS at E_F. The spectrum shown in Fig. 4.6(c) shows finite conductance at 0 mV, while that of the Mott state is approximately zero as shown in Fig. 4.1. Another is the reduction of the size of the gap. Although the Mott gap is approximately 300 meV, the observed gap is reduced to be 200 meV. A possible explanations for these differences is an effect of disorder. A previous theoretical study shows that structural disorder induces the finite DOS and reduction of the effective Mott gap [46]. Another possible explanation is the decrease in the coherence of CDW order due to the existence of the wall, which will be discussed later.

Typical tunneling spectrum taken at the David-stars on the domain wall is shown in Fig. 4.6(c). In contrast to that in the domain, the spectrum on the wall has no peak at negative bias voltage. This seems to indicate the suppression of the Mott gap on the wall. Although the peak at approximately 200 mV remains, the width of the peak is broader than

that in the domain and the corresponding energy is slightly higher than that of the domain. These features of the peak structure suggest that the peak structure seems to have different origin from the UHB, and seems to originate from a resonant state or a band across E_F. Figure 4.6(e) shows variation in the spectra along the arrow on the wall. In contrast to the domain, the conductance at the peak is not periodic, indicating the uniform electronic density of states along the wall.

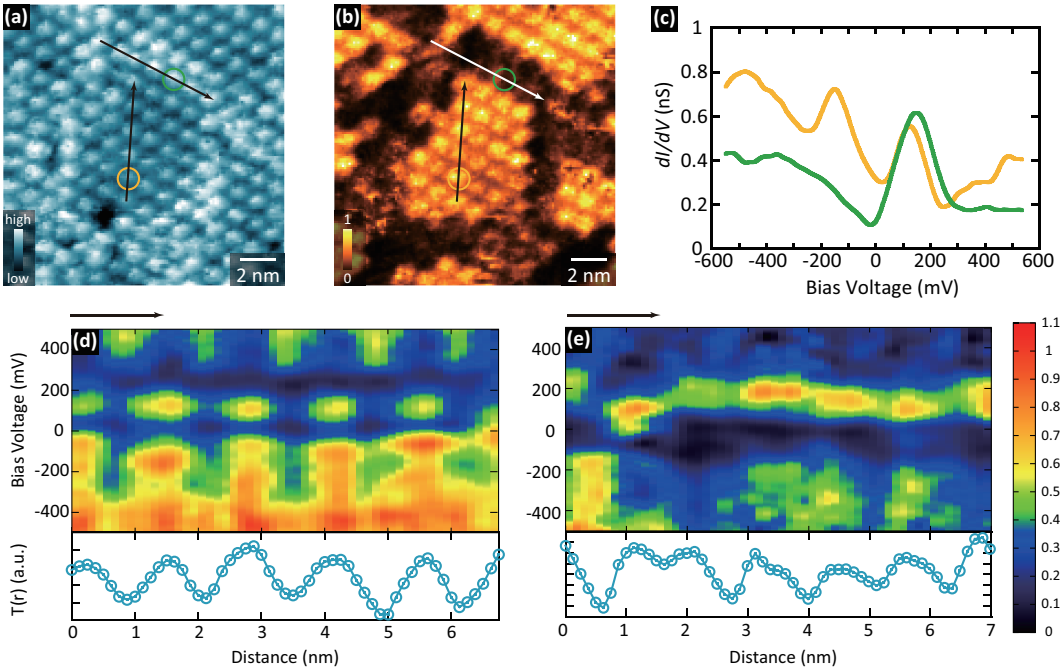

Figure 4.6: STS results of the domain structure. All data are obtained with a set point of 500 mV/200 pA. (a) The STM image where the STS measurement was performed. (b) dI/dV conductance map taken at -100 mV. (c) Tunneling spectra obtained at the David-stars in the domain (orange) and the domain wall (green), shown as circles in (a) and (b). (d), (e) Tunneling spectra along the arrows in the domain and the domain wall, respectively. Lower plots represent the line profiles of the STM topograph along the arrows in the domain and the domain wall.

The observed domain structure in $Ta_{0.99}Fe_{0.01}S_2$ described above has several similarities to the "metallic mosaic" produced by the application of bias voltage pulse [41, 42]: For example, the size of each domain is almost same and the tunneling spectra at each region resemble each other. Thus, the appearance of the domain structure is a universal feature at the melting of the Mott state in $1T$-TaS_2. However, there are several differences between them, specifically the stability of the domain structure. The "metallic mosaic" was reported to disappear with time and as temperature increases to 46 K. However, I observed the same domain structure for at least a few days. Moreover, STM observation on a sample with $x = 0.01$ at 77 K also revealed the existence of the domain structure with size of each domain similar to that at 4.2 K. These facts indicate that the domain structure in Fe doped TaS_2 is more stable than the "metallic mosaic."

A previous STM study of Se substituted TaS_2 revealed the existence of a similar domain structure, and suggested that the domain structure results from stacking of distorted triangular lattices of the David-stars [50]. In Se substituted

TaS_2, the domain structure was observed at approximately 15% substitution, whereas in Fe doped TaS_2, only 1% Fe substitution induces the domain structure. Thus, the stacking of the disordered lattice is not likely to the origin of the domain structure in Fe doped TaS_2, but a rather local effect may cause the domain structure in Fe doped TaS_2. Because ionic radius of Fe is smaller than that of Ta, structural distortion caused by the difference in the ionic radius may induce the domain structure near the Fe site. Another role of Fe on the domain structure is pinning of the walls. Once the domain wall was formed, Fe site possibly pins the wall, resulting in the stabilization of the domain structure even at 77 K. The other candidate of the role of dopant Fe is to provide extra carrier, because the formal valence of Ta and Fe are expected to be 4+ and 2(3)+, respectively. However, we could not find any spectroscopic signature that derived from the difference at present.

STS results in the sample with x=0.02

Figure 4.7(a) and (b) show an STM image and its corresponding dI/dV map at -100 mV of the superconducting $Ta_{0.98}Fe_{0.02}S_2$, respectively. As was seen in Fig. 4.5(c), the David-stars in the STM image shows different contrast. The dI/dV map also indicates the existence of the spatial inhomogeneity of the LDOS, and the area with relatively high conductance correlate to the black contrasted area in the STM image as shown in Fig.4.7(a) and (b). Thus, origin of the inhomogeneity in the STM image is same as that of the dI/dV map. To examine the origin of the inhomogeneity, two spectra were extracted from each region. The spectrum taken at area where the conductance is large (orange one) has two similar peaks to that observed in the domain in the sample with x=0.01 discussed above. On the other hand, the spectrum taken at area where the conductance is small (green one) shows a similar shape to that observed on the wall. These results indicate that the two spectra obtained in this sample is identical to that observed in the domain structure observed in the sample with x=0.01. Thus, the inhomogeneity in the STM image and dI/dV map stems from the electronic difference observed in the domain structure in the sample with x=0.01, though there is no clear domain structure.

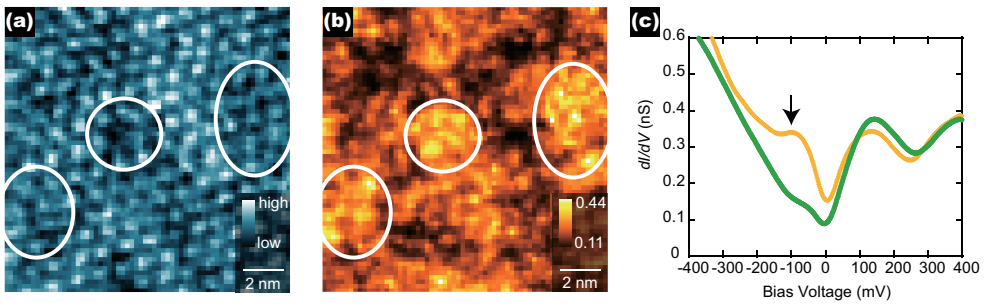

Figure 4.7: Electronic inhomogeneity in superconducting TaS_2 revealed by STS. (a), (b) An STM image and corresponding dI/dV map at -100 mV in a 14 × 14 nm^2 field of view. The set point is 500 mV/200 pA. (c) Tunneling spectra taken at area where conductance at -100 mV is large and small. The arrow in the figure indicates a bias voltage where dI/dV map (b) is taken.

4.4.3 Doping evolution of the electronic states

To investigate the doping evolution of the electronic states, I will present the spatial averaged tunneling spectra of samples with x = 0.01, 0.02, and 0.05 in this section. Figure 4.8 shows the spatially averaged tunneling spectra of samples with x = 0.01, 0.02, and 0.05. With increasing Fe concentration, dI/dV conductance at approximately -100 mV reduces. Because the tunneling spectra, both on the wall and at the David-stars with white contrast in the STM images, has no peak at approximately -100 mV as shown in Fig. 4.6(c) and 4.7(c), the decrease in dI/dV at -100 mV with Fe doping represents the increase in the number of the David-stars that have a electronic state similar to that on the domain wall. In fact, many fragmented domain walls can be seen in the sample with x = 0.02 as shown in Fig. 4.5(c) and 4.7(a). Since the superconductivity emerges at x = 0.02, the increase in the wall regions seems to closely relate to the appearance of the superconductivity.

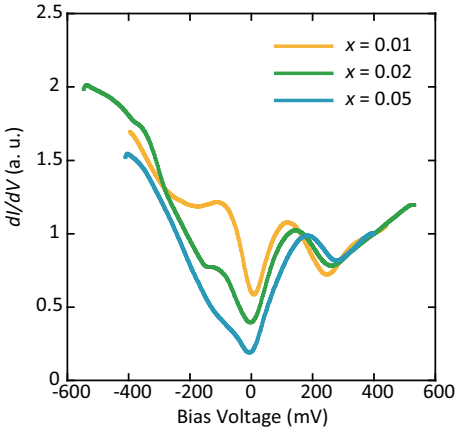

Figure 4.8: Spatially averaged tunneling spectra of the sample with x = 0.01, 0.02, and 0.05. Each spectrum is normalized at 400 mV. As increasing Fe concentration, dI/dV at -100 mV reduces and the energy of the peak structure at positive bias increases.

There are some possible roles of the walls in the appearance of the superconductivity in Fe doped TaS_2. One possibility is that the superconductivity appears at the walls, because the electronic state in the wall has a different nature from that of the domain, which shows the localized nature, as shown in Fig. 4.6(e). The other is that the existence of the wall reduces the coherence of the CCDW. As the CCDW order is strongly tied to the Mott state in $1T$-TaS_2, the wall at which the phase of the CCDW changes sharply reduces the coherence of the CDW and localized nature in the domain. Such a spatial change caused by the wall seems to result in the appearance of superconductivity. Unfortunately, because of the measuring temperature of 4.2 K, the superconducting gap was not measured in this experiment. The measurements of the spatial distribution of the superconducting gap is a future work.

4.5 Summary

STM/STS measurements were performed to investigate how the Mott state evolve with increasing Fe concentration. The surface structure changes from the CCDW state to the anomalous domain structure. The electronic states of the David-stars in the domain shows localized nature, while that in the wall doesn't. When Fe dopant is substituted up to 2 %, obvious domain structure is missing. However, the David-stars which have electronic states similar to that at the walls are observed in addition to the discrete walls. Because the number of the David-stars that have electronic states similar to that at the walls increases, the emergence of the wall must relate to the appearance of superconductivity in this material.

Chapter 5

Summary

I performed STM/STS measurements of $Ir_{1-x}Pt_xTe_2$ and $Ta_{1-x}Fe_xS_2$ in order to understand the role of the dopants and how the SM vanishes when superconductivity appears. In $Ir_{1-x}Pt_xTe_2$, the primary role of dopant Pt is revealed to be local structural distortion, which leads to the formation of the PS. In the case of Fe doped TaS_2, the role of the dopant also is rather structural one, such as local distortion or pinning. Thus, these results indicate that the local strain caused by dopants is important to suppress the SM and induce superconductivity independent on the difference in the electronic structure and the origin of the SM in TMDCs.

In the process how the SM vanishes, I found the appearance of the domain structures in both TMDCs. Very recently, STM/STS study on Cu_xTiSe_2, whose phase diagram is shown in Fig. 1.7(c) revealed the existence of a similar domain structure [48]. In Cu_xTiSe_2, Cu is intercalated between Se layers, whereas in $Ir_{1-x}Pt_xTe_2$ and $Ta_{1-x}Fe_xS_2$, alien element is substituted. Despite the difference, these materials show similar domain structures at the concentration where superconductivity appears. Thus, it seems to be that the formation of domain structure is a common feature among superconducting TMDCs. Further experiments in other TMDCs are expected, such as other polytype.

In this thesis, I performed STM/STS experiments at 4.2 K. Because this temperature is higher than T_c, the direct measurements of superconducting properties, such as the superconducting gap, were not possible. For the further investigation of the relation between the domain structure and the superconductivity, measurements at lower temperature is also expected.

Acknowledgement

I would like to appreciate many people who gave me the substantial support and help in making this thesis. First of all, I would like to thank Prof. Hideaki Sakata who taught me all I know about STM, physics, and way of thought, and gave me a great deal of valuable advice. Without him, none of this study would be possible. Thank also to assistant prof. Satoshi Demura who is my mentor in single crystal growth. He not only taught me the way of crystal growth, but also showed me how to be a physicist and supported my life in doctoral course. Thank also goes to Dr. Machida Tadashi who is my mentor in programming the original software for data analysis. He also taught me the importance of guts for many of experiments. Special thanks goes to National Institute for Material Science members for their useful discussion and help with experiments. Especially, Dr. Kazuto Hirata provided me comfortable environment to evaluate samples. Dr. Takashi Mochiku gave me nice XRD data to compare my STM/STS data. Dr. Shuuichi Ooi also taught me many useful techniques to evaluate samples.

I would like to thank all my labmates for a lot of useful discussion and assistance in single crystal growth and operating STM. Thank to each member for the study in Pt substituted $IrTe_2$, Mr. Kei Igarashi, Mr. Akihiro Kaneko, Mr. Hironori Kariya, Mr. Daiki Morohoshi, and Dr. Hiroshi Nakamura. Thank also to each member for the study in Fe substituted TaS_2, Mr. Tatsunari Shimabukuro, Mr. Kai Kobayashi, Mr. Hiroyuki Kojima, Mr. Shun Ohta, Mr. Takahiro Iwasaki. Thank also to Mr. Katsumi Takano, Mr. Ryuhei Yamamoto, Mr. Ootsuki, Mr. Naoki Ishida, Mr. Ryota Ishio, Mr. Yuto Sakai, Mr. Hiroya Koseki, Mr. Shotaro Shobu, Mr. Daichi Fujii, Mr. Kazuki Miyata. I never forget the important and interesting memories with you.

Finally, I would like to thank my family. To my parents, who supported me mentally and financially, I would like to say thank you for all your supports over many years. Thank also to brothers, who are always makes me laugh and tell me knowledge other than physics. To my wife Ayumi Fujisawa, who kept my mental health very fine, I'd like to say thank you for your all assists in my life.

References

[1] W. L. McMillan, Phys. Rev. B **16**, 643 (1977).

[2] C. M. Varma and A. L. Simons, Phys. Rev. Lett. **51**, 138 (1983).

[3] K. Rossnagel, J. Phys. Cond. Matt. **23**, 213001 (2011).

[4] T. Aruga , Surface Science Reports **61**, 283 (2006).

[5] C. Haas, Solid State Commun. **26**, 709 (1978).

[6] J. E. inglesfield, Physica B **99**, 238 (1980).

[7] F. Weber, S. Rosenkranz, J. -P. Castellan, R. Osborn, R. Hott, R. Heid, K. -P. Bohnen, T. Egami, A. H. Said, and D. Reznik, Phys. Rev. Lett. **107**, 107403 (2011).

[8] C. J. Arguello, S. P. Chockalingam, E. P. Rosenthal, L. Zhao, C. Gutiérrez, J. H. Kang, W. C. Chung, R. M. Ferandes, S. Jia, A. J. Millis, R. J. Cava, and A. N. Pasupathy, Phys. Rev. B **89**, 235115 (2014).

[9] C. Berthier, P. Molinié, and D. Jérome, Solid State Commun. **18**, 1393 (1976).

[10] T. Kiss, T. Yokoya, A. Chainani, S. Shin, T. Hanaguri, M. Nohara, and H. Takagi, Nature Phys. **3**, 720 (2007).

[11] S. Pyon, K. Kudo, M. Nohara, J. Phys. Soc. Jpn., **81**, 053701 (2012).

[12] L. J. Li, W. J. Lu, X. D. Zhu, L. S. Ling, Z. Qu, and Y. P. Sun, Euro. Phys. Lett. **97**, 67005 (2012).

[13] E. Morosan, H. W. Zandbergen, B. S. Dennis, J. W. G. Bos, Y. Onose, T. Klimczuk, A. P. Ramirez, N. P. Ong, and R. J. Cava, Nat. Phys. **2**, 433 (2006).

[14] S. Yan, D. Iaia, E. Morosan, E. Fradkin, P. Abbamonte, and V. Madhavan, Phys. Rev. Lett. **118**, 106405 (2017).

[15] G. Binning, H. Rohrer, Ch. Gerber, and E. Weibel, Phys. Rev. Lett. **49**, 57 (1982).

[16] Y. Kohsaka, C. Taylor, K. Fujita, A. Schmidt, C. Lupien, T. Hanaguri, M. Azuma, M. Takano, E. Eisaki, H. Takagi, S. Uchida, and J. C. Davis, Science **315**, 1380 (2007).

[17] S. H. Pan, E. W. Hudson, and J. C. Davis, Rev. Scientific Inst. **70**, 1459 (1999).

[18] J. J. Yang, Y. J. Choi, Y. S. Oh *et al.*, Phys. Rev. Lett. **108**, 116402 (2012).

[19] K. Kudo, M. Kobayashi, S. Pyon, M. Nohara, J. Phys. Soc. Jpn. **82**, 085001 (2013).

[20] J. J. Yang, Y. J. Choi, Y. S. Oh, A. Hogan, Y. Horibe, K. Kim, B. I. Min, and S-W. Cheong, Phys. Rev. Lett. **108**, 116402 (2012).

[21] H. Cao, B. C. Chakoumakos, X. Chen, J. Yan, M. A. McGuire, H. Yang, R. Custelcean, H. Zhou, D. J. Singh, and D. Mandrus, Phys. Rev. B. **88**, 115122 (2013).

[22] D. Ootsuki, Y. Wakisaka, S. Pyon, K. Kudo, M. Nohara, M. Arita, H. Anzai, H. Namatame, M. Tanigushi, N. L. Saini, and T. Mizokawa, Phys. Rev. B **86**, 014519 (2012).

[23] M. Kamitani, M. S. Bahramy, R. Arita, S. Seki, T. Arima, Y. Tokura, S. Ishiwata Phys. Rev. B **87** 180501 (R) (2013).

[24] A. F. Fang, G. Xu, T. Dong, P. Zheng, and N. L. Wang, Scientific Report 3 1153 (2013).

[25] G.L. Pascut, K. Haule, M. J. Gutmann, S. A. Barnett, A. Bombardi, S. Artyukhin, T. Birol, D. Vanderbilt, J.J. Yang, S.-W. Cheong, and V. Kiryukhin, Phys. Rev. Lett. **112**, 086402 (2014).

[26] T. Toriyama, M. Kobori, T. Konishi, Y. Ohta, K. Sugimoto, J. Kim, A. Fujiwara, S. Pyon, K. Kudo, M. Nohara, J. Phys. Soc. Jpn. **83**, 033701 (2014).

[27] S. Jobic, P. Deniard, R. Brec, J. Rouxel, A. Jouanneaux, and A. N. Fitch, Z. Anorg. Allg. Chem. **598**, 199 (1991).

[28] S. Pyon, K. Kudo, M. Nohara, Physica C **494**, 80 (2013).

[29] T. Mochiku, Y. Matsushita, A. Sato, Y. Fujisawa, K. Igarashi, T. Machida, H. Sakata, K. Hirata, Phys. Procedia **58**, 90 (2014).

[30] D. Ootsuki, T. Toriyama, M. Kobayashi, S. Pyon, K. Kudo, M. Nohara, T. Sugimoto, T. Yoshida, M. Horio, A. Fujimori, M. Arita, H. Anzai, H. Namatame, M. Taniguchi, N. L. Saini, T. Konishi, Y. Ohta, and T. Mizokawa, J. Phys. Soc. Jpn. **83**, 033704 (2014).

[31] A. F. Fang, G. Xu. Dong, P. Zheng, and N. L. Wang, Scientific Reports **3**, 1153 (2013).

[32] T. Machida, Y. Fujisawa, K.Igarashi, A. Kaneko, S. Ooi, T. Mochiku, M. Tachiki, K. Komori, K. Hirata, and H. Sakata, Phys. Rev. B **88**, 245125 (2013).

[33] R. E. Thomson, B. Burk, A. Zettl, and J. Clarke, Phys. Rev. B **49**, 899 (1994).

[34] J.-J. Kim, W. Yamaguchi, T. Hasegawa, and K. Kitazawa, Phys. Rev. Lett. **73**, 2103 (1994).

[35] X. L. Wu and C. M. Lieber, Phys. Rev. Lett. **64**, 1150 (1990).

[36] D. Cho, Y.-H. Cho, S.-W. Cheong, K.-S. Kim, and H. W. Yeom, Phys. Rev. B **92**, 085132 (2015).

[37] L. perfetti, P. A. Loukakos, M. Lisowski, U. Bovensiepen, M. Wolf, H. Berger, S. Biermann, and A. Georges, New J. Phys. **10**, 053019 (2008).

[38] Y. Liu, R. Ang, W. J. Lu, W. H. Song, and Y. P. Sun, App. Phys. Lett. **102**, 192692 (2013).

[39] L. Stojchevska, I. Vaskivskyi, T. Mertelj, P. Svetin, S. Brazovskii, and D. Mihailovic, Science **344**, 177 (2014).

[40] I. Vaskivskyi, J. Gospodaric, S. Brazovskii, D. Svetin, P. Sutar, E. Goreshnik, I. A. Mihailovic, T. Mertelj, D. Mihailovic, Sci. Adv. 1:e1500168 (2015).

[41] L. Ma, C. Ye, Y. Yu, X. F. Lu, X, Niu, S. Kim, D. Feng, D. Tomânek, Y -W. Son, X. H. Chen, and Y. Zhang, Nat. commun. **7**, 10956 (2016).

[42] D. Cho, S. Cheon, K -S. Kim, S -H. Lee, Y -H. Cho, S -W. Cheong, H. W. Yeom, Nat. Commun. **7**, 10453 (2016).

[43] R. Ang, Y. Tanaka, E. Ieki, K. Nakayama, T. Sato, L. J. Li, W. J. Lu, Y. P. Sun, and T. Takahashi, Phys. Rev. Lett. **109**, 176403 (2012).

[44] F. J. Di Salvo, J. A. Wilson, and J. V. Waszczak, Phys, Rev. Lett. **36**, 885 (1976).

[45] H. Chen, X. L. Wu, and C. M. Lieber, J. Am. Chem. Soc. **112**, 3326 (1990).

[46] E. Lahoud, O. N. Meetei, K. B. Chaska, A. Kanigel, and N. Trivedi, Phys. Rev. Lett. **112**, 206402 (2014).

[47] T. Endo, W. Yamaguchi, O. Shiino, T. Hasegawa, and K. Kitazawa, Sur. Sci. **453**, 1 (2000).

[48] S. Yan, D. Iaia, E. Morosan, E. Fradkin, P. Abbamonte, and V. Madhavan, Phys. Rev. Lett. **118**, 106405 (2017).

[49] Y. Liu, R. Ang, W. J. Lu, W. H. Song, and Y. P. Sun, App. Phys. Lett. **102**, 192692 (2013).

[50] D. Fujii, T. Iwasaki, K. Akiyama, Y. Fujisawa, S. Demura, H. Sakata, To be published in J. Phys: Conf. Series.

[51] L. Li, X. Deng, Z. Wang, Y. Liu, M. Abeykoon, E. Dooryhee, A. Tomic, Y. Huang, J. B. Warren, E. S. Bozin, S. J. L. Billinge, Y. Sun, Y. Zhu, G. Kotliar, C. Petrvic, npj Auantum Mat. **2**, 11 (2017).

[52] K. Momma, F. Izumi, J. Appl. Crystallogr. **44**, 1272 (2011).